Biomedicine & Pharmacotherapy 155 (2022) 113723

Contents lists available at ScienceDirect

Biomedicine & Pharmacotherapy

journal homepage: www.elsevier.com/locate/biopha

Colon cancer therapy with calcium phosphate nanoparticles loading bioactive compounds from *Euphorbia lathyris*: *In vitro* and *in vivo* assay

Cristina Mesas [a,b,c,1], Víctor Garcés [d,1], Rosario Martínez [e], Raúl Ortiz [a,b,c], Kevin Doello [f], Jose M. Dominguez-Vera [d], Francisco Bermúdez [g], Jesús M. Porres [e], María López-Jurado [e], Consolación Melguizo [a,b,c,*], José M. Delgado-López [d,2], Jose Prados [a,b,c,2]

[a] Institute of Biopathology and Regenerative Medicine (IBIMER), Center of Biomedical Research (CIBM), University of Granada, 18100 Granada, Spain
[b] Department of Anatomy and Embryology, Faculty of Medicine, University of Granada, 18071 Granada, Spain
[c] Instituto de Investigación Biosanitaria de Granada (ibs.GRANADA), 18014 Granada, Spain
[d] Department of Inorganic Chemistry, Faculty of Science, University of Granada, 18071 Granada, Spain
[e] Department of Physiology, Institute of Nutrition and Food Technology (INyTA), Center of Biomedical Research (CIBM), University of Granada, 18100 Granada, Spain
[f] Medical Oncology Service, Virgen de las Nieves Hospital, 18014 Granada, Spain
[g] Cellbitec S.L., N.I.F. B04847216, Scientific Headquarters of the Almería Technology Park, Universidad de Almería, La Cañada, 04128 Almería, Spain

ARTICLE INFO

Keywords:
Calcium phosphate nanoparticles
Euphorbia lathyris
Colon cancer
Esculetin
Euphorbetin

ABSTRACT

Amorphous calcium phosphate nanoparticles (ACP NPs) exhibit excellent biocompatibility and biodegradability properties. ACP NPs were functionalized with two coumarin compounds (esculetin and euphorbetin) extracted from *Euphorbia lathyris* seeds (BC-ACP NPs) showing high loading capacity (0.03% and 0.34% (w/w) for esculetin and euphorbetin, respectively) and adsorption efficiency (2.6% and 33.5%, respectively). BC-ACP NPs, no toxic to human blood cells, showed a more selective cytotoxicity against colorectal cancer (CRC) cells (T-84 cells) (IC50, 71.42 μg/ml) compared to non-tumor (CCD18) cells (IC50, 420.77 μg/ml). Both, the inhibition of carbonic anhydrase and autophagic cell death appeared to be involved in their action mechanism. Interestingly, in vivo treatment with BC-ACPs NPs using two different models of CRC induction showed a significant reduction in tumor volume (62%) and a significant decrease in the number and size of polyps. A poor development of tumor vasculature and invasion of normal tissue were also observed. Moreover, treatment increased the bacterial population of Akkermansia by restoring antioxidant systems in the colonic mucosa of mice. These results show a promising pathway to design innovative and more efficient therapies against CRC based on biomimetic calcium phosphate NPs loaded with natural products.

1. Introduction

The high incidence of colorectal cancer (CRC), the third most frequent cancer worldwide, has been related to sedentary lifestyle, nutrition and population aging [1,2]. Surgical treatment is commonly used in non-metastatic CRC [3], but chemotherapy is still required in advanced (metastatic) cancer. Despite monoclonal antibodies and multiple kinase inhibitors have significantly improved the prognosis of CRC in recent years [4], the success of chemotherapy still depends on the development of new anticancer agents and transport systems. In this context, the use of nanoparticles (NPs) as drug carriers can improve drug solubility, avoid multidrug resistance mechanisms (i.e. P-glycoprotein), and allow the active targeting of tumor cells through NPs functionalization, enhancing cell internalization and selectivity [5,6]. In addition, NPs can increase the retention of drugs in tumor tissues in relation to healthy tissues, decreasing their toxicity [7]. This differential behavior can be essentially explained by the enhanced permeability and retention effect (EPR), which has been related to the presence of fenestrated and more permeable blood vessels and inefficient lymphatic drainage [8–10].

* Corresponding author at: Institute of Biopathology and Regenerative Medicine (IBIMER), Center of Biomedical Research (CIBM), University of Granada, 18100 Granada, Spain.
E-mail address: melguizo@ugr.es (C. Melguizo).
[1] Equal contribution
[2] Co-senior authors equal contribution

https://doi.org/10.1016/j.biopha.2022.113723
Received 27 July 2022; Received in revised form 15 September 2022; Accepted 19 September 2022
Available online 23 September 2022

Among the wide variety of reported NPs, calcium phosphates NPs, the main inorganic component of mammals hard tissues (e.g., bone and teeth), are very promising owing to their remarkably biocompatibility and biodegradability [11,12]. Indeed, nanocrystalline apatite (Ap), or its precursor, amorphous calcium phospahte (ACP) have been widely used as bioactive components of bioceramics for tissue regeneration [13–15]. The lack of toxicity, low-cost synthesis and pH-dependent solubility (i.e., slightly soluble at acidic pHs) are also very attractive features for the controlled delivery of active species. Moreover, the high surface reactivity of these NPs favours the electrostatic or chemical interaction with a large variety of molecules [16]. By finely tuning the experimental conditions, the surface of the NPs can be specifically enriched with molecules exerting antitumor activity or cell targeting [17,18]. The pH-dependent dissolution of the NPs allows the gradual release of the adsorbed bioactive compounds at slightly acidic pHs, for instance as that usually found at the microenvironment of the tumours [19]. For all of these reasons, calcium phosphate NPs are a smart alternative to metallic nanoparticles such as gold, silver or iron oxide nanoparticles, which have more limited biocompatibility and more expensive bioconjugation [20].

On the other hand, different plant extracts from various species are being recognized as a rich source of antioxidant compounds, including polyphenols and flavonoids [21]. Besides, they are excellent sources of bioactive compounds with different health benefits such as antitumor, antifungal and/or antibiotic properties, derived from their specific structure [22–24]. The biological activity of natural extracts depends on the specific action of each of the bioactive compounds and the appearance of synergistic effects between them [25]. Thus, the efficacy and therapeutic effect of a natural extracts can be modulated by controlling the relative concentrations of the bioactive compounds present in it [26]. The high incidence of cancer worldwide has aroused enormous interest in the search of new natural extracts with potential to prevent and suppress cancer proliferation [27,28]. *Euphorbia*, a therapeutic resource of traditional Chinese medicine, has attracted great interest for its recognized anticancer properties. Some natural extracts derived from *Euphorbia* exhibit antitumor and anti-inflamatory properties, which have been attributed to secondary metabolites belonging to different biochemical compounds, including polyphenols, flavonoids, sterols, terpenes and coumarins [29]. Remarkably, different parts (e.g., roots, seeds, latex, wood, barks and leaves) from plants of the genus *Euphorbia* have been used in traditional medicine all over the world [30]. In recently published studies, we obtained and characterized a functional extract from the seeds of *Euphorbia lathyris* [31]. This polyphenol-rich extract presented very strong antitumor activity against different CRC cell lines through molecular mechanisms related to apoptosis and autophagy activation. Likewise, the presence of two polyphenolic compounds (esculetin and euphorbetin) responsible for the antitumor activity of this extract was confirmed [31].

Interestingly, esculetin, a natural coumarin derivate, has been found in various plants of the genus *Euphorbia* [32], both combined and separated from its dimer (i.e., euphorbetin), which has also been identified in some *Euphorbia* species [31,33]. The antiproliferative and apoptotic response in several cancer cell lines treated with esculetin have been previously reported in studies aimed at developing new cancer therapies. In addition, anticoagulant activity of both coumarin derivates has been demonstrated [34–36]. Apart from the antitumor and anticoagulant activity of esculetin, this dihydroxycoumarin derivate produces multiple pharmacological effects, including anti-inflamatory, antioxidant, hepatoprotective, antidiabetic, actibacterial, and adipogenesis suppressor [37]. The adsorption of these bioactive molecules on the surface of the NPs could increase their intrinsic therapeutic effects. Moreover, NPs could prevent the degradation of these molecules by cellular metabolism and thus improve their biodistribution and bioavailability [38,39].

With this in mind, the aim of this study was to design a drug delivery nanosystem consisting of non-toxic biodegradable ACP NPs loaded with antitumor molecules from seed extracts of *Euphorbia lathyris* to improve their antitumor effect in CRC. We hypothezed that this new nanosystem could increase the esculetin and euforbetin entry into tumor cells, increasing their antitumor CRC cell effect. *In vitro* and in vivo assays using human colon carcinoma cells and two animal models of CRC demonstrated that this new strategy may represent an advance in the treatment of CRC and may be a strong candidate to the development of future clinical trials.

2. Methods

2.1. Reagents

Calcium chloride dihydrate ($CaCl_2 0.2\ H_2O$, Bioxtra, ≥99.0% pure), sodium citrate tribasic dihydrate ($Na_3(Cit)\cdot 2\ H_2O$, where Cit = citrate = $C_6H_5O_7$, ACS reagent, ≥ 99.0% pure), potassium phosphate dibasic (K_2HPO_4, ACS reagent, ≥99.0% pure) and sodium carbonate monohydrate ($Na_2CO_3\cdot H_2O$, ACS reagent, 99.5% pure) were purchased from Sigma–Aldrich. Ultrapure water (0.22 μS, 25 °C, MilliQ©, Millipore) was used to prepare all solutions. *Euphorbia* seeds were supplied by CellBiTec S.L. (Almería, Spain). The standards of esculetin and euphorbetin were purchased from Biopurify Phytochemicals Ltd. (Chengdu, Sichuan, China). The purity of each reference standard was determined to be higher than 98% by HPLC. HPLC-grade acetonitrile was purchased from Merck (Darmstadt, Germany). HPLC-grade acetic acid from Sigma-Aldrich (Steinheim, Germany).

2.2. Synthesis of biomimetic nanoparticles

ACP NPs were synthesized following a precipitation method previously reported by Delgado-López et al. with modifications [11]. Two solutions (1:1 v/v, 100 ml total) of (a) 0.12 M K_2HPO_4 + 0.1 M Na_2CO_3 and (b) 0.2 M $CaCl_2$ + 0.2 M Na_3(cit) were mixed and were continuously stirred at around 250 rpm using a stirring hot plate for about 5 min at room temperature. Afterwards, the precipitates (ACP NPs) were repeatedly washed with ultrapure water by centrifugation to remove unreacted salts.

2.3. ACP Functionalization

ACP NPs (100 mg) were suspended in 5 ml of ultrapure water and sonicated for 30 min in an Allendale-Ultrasonic cleaner. 100 mg of *Euphorbia* extract previously dissolved in a mixture of ethanol: water: HCl (50: 50: 0.25, v/v/v), was added to the latter suspension. The mixture was stirred at room temperature for 24 h in the dark to avoid photolytic decomposition of bioactive compounds (BC) of the extract. Subsequently, functionalized nanoparticles (hereafter referred to as BC-ACP) were separated from unbound compounds by centrifugation at 10.000 rpm for 5 min. Afterwards BC-ACP were carefully washed three times with 10 ml of ultrapure water to remove the weakly bounded bioactive molecules. A blank sample was also prepared. ACP (100 mg) were incubated during 24 h in the mixture of ethanol: water: HCl (50: 50: 0.25, v/v/v). Then, the same protocol as BC-ACP was followed to collect blank NPs.

2.4. Characterization of the nanoparticles

The precipitates of the ACP and BC-ACP were characterized by FTIR spectroscopy, PXRD and transmission electron microscopy (TEM). Ca/P ratio was quantified by inductively-coupled plasma optical emission spectroscopy (ICP-OES). FTIR spectra were recorded on a Bruker Tensor 27 FTIR Spectrometer in transmission mode using KBr pellets. Each pellet was prepared by mixing 3 mg of powdered sample with 200 mg of anhydrous KBr and pressed into 7 mm diameter discs. Pure KBr discs were used as background. FTIR spectra were registered from 4000 cm^{-1} to 400 cm^{-1} with a resolution of 4 cm^{-1}.

PXRD patterns of the samples were collected using a Bruker D8 Advance diffractometer equipped with a Lynx-eye position sensitive detector using Cu Kα radiation (λ = 1.54178 Å) generated at 40 kV and 40 mA. Diffractograms were recorded in the 2θ range from 15° to 70° with a step size (2θ) of 0.02 and a counting time of 1 s

TEM analyses were performed with a Carl Zeiss SMT LIBRA 120 PLUS microscope operating at 120 kV. The powder samples were ultrasonically dispersed in ultrapure water using an Allendale-Ultrasonic cleaner and then few droplets of the slurry were deposited on mesh copper TEM grids covered with thin amorphous carbon films and incubated for several minutes.

The Ca/P ratio of the samples was determined by ICP-OES. To determine the chemical composition, the powder samples were dissolved in a diluted HNO3 solution (1 wt%) and then analyzed by a PERKIN-ELMER OPTIMA 8300 ICP-OES Spectrometer employing wavelengths of 422.673 nm (Ca) and 213.618 nm (P). The analyses were carried out three times for each sample.

2.5. Characterization of the Euphorbia lathyris seed extract

The ethanolic extract was generated from mature seeds of E. lathyris (variety S3201), transferred by Agrointec Solitions S.L (Almería, Spain). Before the procedure, seeds were defatted by CELLBITEC S.L. Later, the ethanolic extract was developed following our own protocol [31].

Identification of bioactive compounds that are part of the *Euphorbia lathyris* extract was achieved by means of ultra-high-performance liquid chromatography-electrospray ionization tandem mass spectroscopy (UPLC-ESI(-)-MS). The chromatographic method was the same as latter described for identification of bioactive compounds adsorption on NPs (Section 2.6). The identification of major active ingredients from *Euphorbia* extract was based on their retention times (RT) and mass (MS) fragments.

Besides the UPLC-MS analysis, *Euphorbia* extract was characterized by UV–vis spectroscopy. UV–vis spectrum of *Euphorbia* extract was recorded at a Unicam UV 300 Thermo Spectronic spectrophotometer. The UV–vis spectra of the most interesting bioactive compounds, esculetin and euphorbetin, exhibited an absorbance band-centred at 344 nm (ε^{344} =60.2 mg ml^{-1} cm^{-1}) [40,41].

Ultra-high-performance liquid chromatography coupled to a Diode array detection (UPLC-DAD) was employed for quantifying bioactive compounds from *Euphorbia* extract. Plant extract was filtered through 0.22 μm nylon disk filters and 10 μl of filtered extract was injected into the chromatograph. Analytical separation was carried out in the same conditions as the quantification of bioactive compounds adsorption on NPs (Section 2.6).

2.6. Identification and quantification of bioactive compounds adsorption on NPs

The identification of the bioactive compounds adsorbed on the NPs was carried out by Ultra-Performance Liquid Chromatography (Acquity H Class, Waters) tandem orthogonal acceleration time-of-flight mass spectrometer (LCT Premier XE, Waters) with an electrospray-ionization (ESI) technique (UPLC-ESI(-)-MS). BC-ACP (1 mg) were partially decomposed in an acidic solution (pH=3) by stirring during 24 h. Partial dissolution of BC-ACP ensure the release of adsorbed molecules on NPs surface. After release, 10 μl of the final dissolution of functionalized NPs, previously filtered through 0.22 μm nylon disk filters (Millipore), were injected into the chromatograph. Analytical separation of bioactive compounds was performed on a Waters CORTECS™ C18 column (100 mm x 2.1 mm internal diameter, 1.6 μm) at room temperature. A mobile phase consisting in a gradient program combining deionized water with 0.5% of acetic acid as solvent A and acetonitrile as solvent B was used. The initial conditions were 90% A and 10% B. A linear gradient was then established to reach 100% (v/v) of B at 5 min. Total run time was 8 min. Mobile phase flow rate was 0.3 ml/min. After chromatographic separation, a high-resolution mass spectrometry analysis was carried out in negative electrospray ionization (ESI -). The gas used for desolvation (500 L h^{-1}) and cone (50 L h^{-1}) was high-purity nitrogen. Spectra were recorded over the mass/charge (m/z) range of 100–1200. All the compounds were identified based on their retention times (RT) and mass (MS) fragments. Based on these data, the compounds were tentatively identified using MassLynx software.

The analytical quantification of the adsorbed bioactive compounds was performed by Ultra Performance Liquid Chromatography (Acquity UPLC-I Class. Waters) coupled to a Diode Array Detection (Acquity TUV Detector) (UPLC-DAD). BC-ACP (1 mg) were partially dissolved in an acidic solution (pH=3) by stirring during 24 h to ensure complete release of adsorbed bioactive compounds. Dissolution of functionalized NPs was filtered through 0.22 μm nylon disk filters (Millipore) and analyzed. 10 μl of filtered solution was injected into the chromatograph. Analytical separation of bioactive compounds was performed on a Waters CORTECS™ C18 column (100 mm x 2.1 mm internal diameter, 1.6 μm) at room temperature. A mobile phase consisting in a gradient program combining deionized water with 0.5% of acetic acid as solvent A and acetonitrile as solvent B was used. The initial conditions were 90% A and 10% B. A linear gradient was then established to reach 100% (v/v) of B at 5 min. Total run time was 8 min. Mobile phase flow rate was 0.3 ml/min. The concentrations of BC were evaluated from peak areas at 344 nm, using external calibration curves established with the corresponding standards, esculetin and euphorbetin. Once, the amounts of adsorbed BC were measured, the adsorption efficiency (AE) and loading capacity (LC) were calculated as follows:

$$AE = \frac{weight\ \ of\ \ adsorbed\ \ BC}{total\ \ weight\ \ BC\ \ in\ \ Euphorbia\ \ Extract} x100 \quad (1)$$

$$LC = \frac{weight\ \ of\ \ adsorbed\ \ BC\ \ (mg)}{weight\ \ of\ \ nanoparticles\ \ (g)} \quad (2)$$

2.7. Release of bioactive compounds from BC-ACP

In order to assess the cumulative release of BC from BC-ACP ($C_{R,}$ %), the time-dependent release of BC from BC-ACP was analyzed at two physiological pH conditions. At a pH of 7.4, the physiological pH of blood and at a pH of 5.5, simulating the pH inside cell lysosomes (pH~5).[17] 15 mg of BC-ACP were immersed in Phosphate Buffered Saline (PBS, 10 mM, 3 ml, pH 7.4) and in Sodium Citrate Buffer (10 mM, 3 ml, pH 5.5), respectively, at room temperature. The relative amount of released bioactive compound was measured recording UV-Vis spectra of the suspensions every 30 min during 9 days. The UV–vis spectra of the most interesting bioactive compounds, esculetin and euphorbetin, exhibited an absorbance band-centred at 348 nm in Sodium Citrate Buffer (pH 5.5) and at 366 nm in Potasium Phosphate Buffer (pH 7.4). After 9 days, the release of BC from BC-ACP was complete, which was considered the absorbance corresponding to the drug loading capacity (Q_{max}) of BC-ACP. Q_t represents the absorbance corresponding to the amount of drug released at time t. Cumulative release curves were obtained according to Eq. 3. Release data were further fitted to first order kinetic models to obtain the release rates at two physiological pH conditions (K).

$$C_R = \frac{Q_t}{Q_{max}} x100 \quad (3)$$

To ensure that the release of adsorbed bioactive compounds from BC-ACP was complete after 9 days (Q_{max}), the remaining ACP after 9 days of release were decomposed in an acidic solution (pH=3) by stirring during 24 h. After complete decomposition, 10 μl of the final dissolution of released-functionalized NPs were injected into the chromatograph to identify the remaining bioactive compounds after the release process. The chromatographic method was the same as described above for the identification of the adsorption of the bioactive compounds on NPs

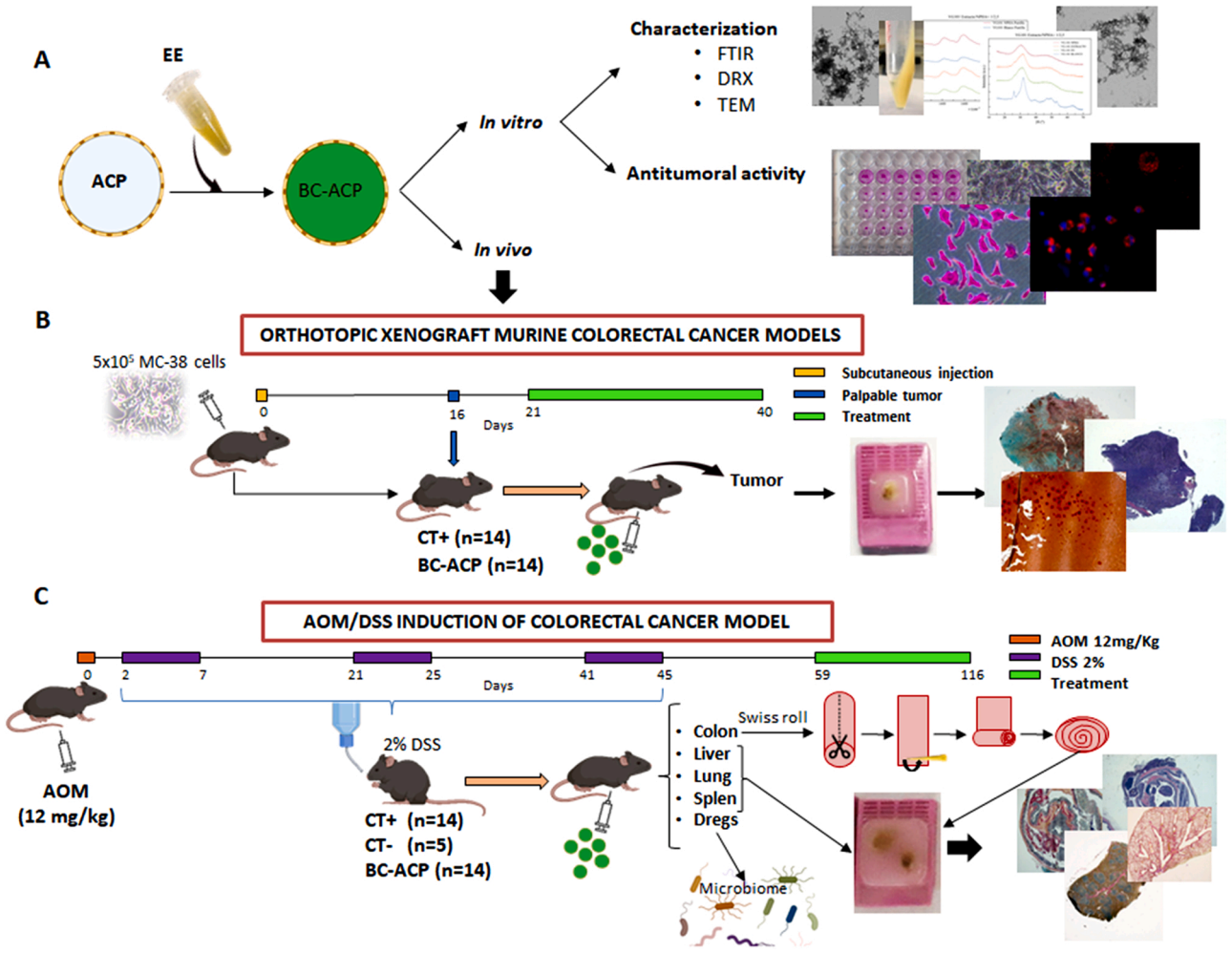

Fig. 1. Schematic representation of the in vitro (A) and in vivo assay using two CRC induction models. (B) Orthotopic xenograft murine CRC cancer model. When the subcutaneous tumor was palpable (16 days after inoculation of MC-38 cells), treatment with BC-ACP was applied during 19 days using an intraperitoneal injection every 3 days. After the end point of experiment, mice were sacrificed and tumor sample were obtained for histological analysis. (C) AOM/DSS induction of CRC cancer model. After administration of AOM and DSS agents, colon cancer was induced for 59 days. By intraperitoneal injection every 3 days for 57 days, BC-ACP was administered. As in the other subcutaneous induction model, after mice sacrifice, tumor in colon and organs were obtained for histological analysis. In this case, the Swiss-roll technique was carried out to preserve the colon and to perform histological analysis.

(Section 2.6). In this case, UPLC-ESI(-)-MS total ion current chromatograms revealed any signals associated to the compounds of interest (Fig. 6), confirming the complete release of BC from BC-ACP after 9 days.

2.8. Colon cancer cell cultures

The human colon adenocarcinoma cell line T84 and murine colon adenocarcinoma cell line MC-38 were purchased from the American Type Culture Collection (Rockville, MD, USA). The non-tumor colon cell line CCD18 (human colon epithelial cell line) was used as control. For culture, cells were grown in Dulbecco's Modified Eagle's Medium (DMEM) (Sigma-Aldrich, Madrid, Spain) supplemented with 10% fetal bovine serum (FBS) (Gibco, Madrid, Spain) and 1% ATB (antibiotic, streptomycin + amphotericin B). Cells were maintained in an incubator at 37 ºC and 5% CO_2 humidified atmosphere.

2.9. Proliferation assay

Cells were seeded in 48-well plates with DMEM (Dulbecco's modified Eagles Medium) (300 µl) at a density of 4×10^3 cells/well in CCD18 and 5×10^3 cells/well in T84. After 24 h, cell cultures were exposed 72 h to increasing concentrations of the NPs dissolved in DMEM. In addition, bioactive components of the extract, Esculetin (range from 0,1 µg/ml to 5 µg/ml) and Euphorbetin (range from 0.02 µg/ml to 0.7 µg/ml), were combined at different concentration in order to determine their antitumor activity and to compare with NPs activity and ethanolic extract activity. After incubation time, cells were fixed with 10% trichloroacetic acid (TCA) and stained with 0.4% sulforhodamine B (SRB) in 1% of acetic acid. Finally, the SRB was solubilized with Trizma® (10 mM, pH 10.5) and the optical density (OD) was measured at 492 nm in a spectrophotometer EX-Thermo Multiskan. For calculate cell survival (%), the following equation was applied:

$$Cell\ \ survival\ \ (\%) = \frac{Treated\ \ cells\ \ OD - blank}{Control\ \ OD - blank}\ x\ 100 \qquad (4)$$

Furthermore, IC_{50} was calculated with GraphPad Prism 6 Software (La Jolla, CA, USA).

2.10. Blood cell compatibility of ACP, BC-ACP

2.10.1. Hemolysis assay

This assay was carried out from human blood. For that, a healthy donor gave 25 ml of blood (collection tubes with EDTA) (Andalusian Public Health System Biobank) and following our own protocol the

assay was performance [42]. Firstly, erythrocytes were diluted (1:50) (pH 7.4) and 190 μl was added to 96-well plates. In the same way, BC-ACP was added at different concentrations (12–976 μg/ml) in a volume of 10 μl per well. As positive control, Triton X-100 (10 μl; 20%) was used and like negative control phosphate buffer pH 7.4 (10 μl) was used. Finally, the plate was incubated (1 h at 37 °C with shaking (15 rpm), centrifuged (500xg for 5′), and the supernatant (100 μl) was transferred to another 96-well plate. For calculate the percentage of hemoglobin released by erythrocytes, it was determined by spectrophotometry (wavelength of 492 nm) with a Titertekmultiscan colorimeter (492 nm) (Flow, Irvine, California) and the next formula was used:

$$Hemolysis\ (\%) = \frac{abs.\ of\ the\ sample - abs.\ of\ the\ negative\ control}{abs.\ of\ the\ positive\ control} x\ 100 \quad (5)$$

Images of erythrocytes exposed to different treatment were taken to analyze morphological changes.

2.10.2. Peripheral lymphocyte assay

As in the hemolysis assay, with the same blood from healthy donors. White blood cells (WBCs) were isolated using Ficoll-Paque (v/v) following our own protocol [43]. 2×10^4 cells/well were cultured in 96-well plates (90 μl). BC-ACP (10 μl) was added to each well at different concentration from 12 to 976 μg/ml and were incubated for 1 and 12 h at 37 °C and 5% CO2 in a humidified atmosphere. Finally, the viability of WBCs was determined by the Cell Counting Kit-8 (CCK-8) (Sigma-Aldrich, Saint Louis, MO, USA). For that, cells were incubated 3 h with CCK-8 solution (10%) and absorbance (450 nm) was measured using a microplate reader.

2.11. Lysotracker Labeling

To determinate vesicles of autophagy or internalizing vesicle in living cells, LysoTracker® Red DND-99 (Thermo Fisher Scientific, USA) is used due to it is a fluorescent red dye that label and monitories acidic organelles. To determine it, cultures of T-84 cells were exposed to the NPs (IC_{50}) during 24 h. After that, cells were washed in PBS and loaded with Lysotracker 50 nM (30 min at 37 ºC). Finally, cells were stained with DAPI (1:1000) and observed under the fluorescence microscope.

2.12. In vivo assays

To carry out both in vivo experiments, brown female C57BL/6 mice (weight 18–20 g, 6 weeks old) (Charles River Laboratories Inc, Wilmington, MA, USA) were used. Mice were housed in colony cages with light and temperature controlled (22 ºC, and 12 h light–dark cycle) and with free access to water and food. In addition, all animal studies were approved by the Ethics Committee on Animal Experimentation of the University of Granada (Reference code: 16/01/2020/005) and in accordance with international standards (European Communities Council Directive 2010/63).

2.12.1. Orthotopic xenograft murine colorectal cancer models

Subcutaneous tumors were induced injecting into the right flank of the mice 5×10^5 cells of the MC38 cell line resuspended in 100 μl of PBS. When tumors were palpable (2×2 mm), mice were randomly divided into 2 groups (n = 14): a control group (CT+) and a group treated with BC-ACP. Treatment (10 μl Bc-ACP / g mice, equivalent to 1,5 ng sculetin / g mice and 17 ng Euphorbetin / g mice) was administered by intraperitoneal injection every 3 days for a total of 7 doses. The weight and tumor growth of the animal were controlled with a balance and measuring tumor dimensions with a digital caliper every 3 days. Tumor volume (mm^3) was calculated using the following formula:

$$V\ \left(mm^3\right) = \frac{a\ x\ b^2\ x\ \pi}{6} \quad (6)$$

where "a" is the largest diameter of the tumor, and "b" is the largest diameter perpendicular to "a". Day 40 from the inoculation of tumor cells was the end point of the experiment and the sacrifice of mice by anesthetic with isoflurane (Sigma-Aldrich, Madrid, Spain) inhalation and complete removal of all blood from the mouse via axillary vessels. Finally, samples from tumor and different organs (liver, lung and spleen) were obtained for inclusion in paraformaldehyde (Fig. 1B).

2.12.2. Azoxymethane (AOM)/Dextran Sodium Sulfate (DSS) induction of colorectal cancer model

Mice (n = 28) were treated with a single intraperitoneal injection of AOM (12 mg/kg) (Sigma-Aldrich, Madrid, Spain). After 48 h, mice were treated with 3 cycles of DSS (Sigma-Aldrich, Madrid, Spain) dissolved in water for 5 days/cycle. Between cycles, a rest period (15 days) with normal water was taken. The first and second cycles were with 2% DSS and the thirst cycle with 3% DSS. During this period of induction, the weight of mice was controlled. After the last 15 days of rest, mice were randomly allocated into two groups (n = 14): a group control (CT+) and a group treated with BC-ACP. In addition, a third group (n = 5) was formed with healthy mice (CT-). During the treatment all groups of mice had free access to water and food. Treatment with BC-ACP (10 μl/g) was administered by intraperitoneal injection every 3 days for a total of 19 doses. The end point of the experiment was on the 116th day from injection of AOM by anesthetic with isoflurane (Sigma-Aldrich, Madrid, Spain) inhalation and complete removal of all blood from the mouse via axillary vessels. Samples of different organs (liver, lung and spleen) were obtained for inclusion in paraformaldehyde. In this case, colon samples were included using the Swiss-rolling technique (Fig. 1C) [44].

2.13. Morphological and histological analysis: polyps size and distribution

Once the colon of mice was obtained by incision, opened and photographed, ImageJ was used to count and measure polyps. To fix samples from tumor, organs and Swiss-roll paraformaldehyde (24 h) was used. Then, they were included in paraffin blocks to obtain 5 μm sections with a rotary microtome (Leica, Wetzlar, Germany). After deparaffinizing and hydrating, the sections were stained with hematoxylin-eosin (H&E) and pentachrome methods [45]. These images were obtained with a photographic microscope (Nikkon Eclipse Ni, Melville, USA).

2.14. Carbonic anhydrase analysis in tumor

Carbonic anhydrase activity was carried out from cancer tissue. For that, samples from subcutaneous tumors of different treatment (CT+ and BC-ACP), conserved in liquid nitrogen previously, were homogenized and processed following the protocol described by Gai et al. (2014) [46]. Briefly, homogenized samples (2 μg of total protein) were mix with cold carbonated water and as colorimetric pH marker, phenol red was chosen. Finally, absorbance was measured at 557 nm using a spectrophotometer (Titertekmultiscan colorimeter, Flow, Irvine, California).

2.15. Hematological toxicity analysis

To corroborate hemocompatibility of BC-ACP and evaluate the possible toxicity, 1 ml/animal of mice blood was obtained. For that, mice were anesthetized and blood was collected by cardiac puncture. The hemogram was processed in Mslab21 Medical Lab Fully Auto Hematology Analyzer/Cbc Test Machine (Medsinglong Global Group Co, China).

2.16. DNA extraction and bacterial identification in cecal samples

After the end point of experiment, colon content was collected to determine the microbiota profiling and obtain the genomic DNA (Gdna)

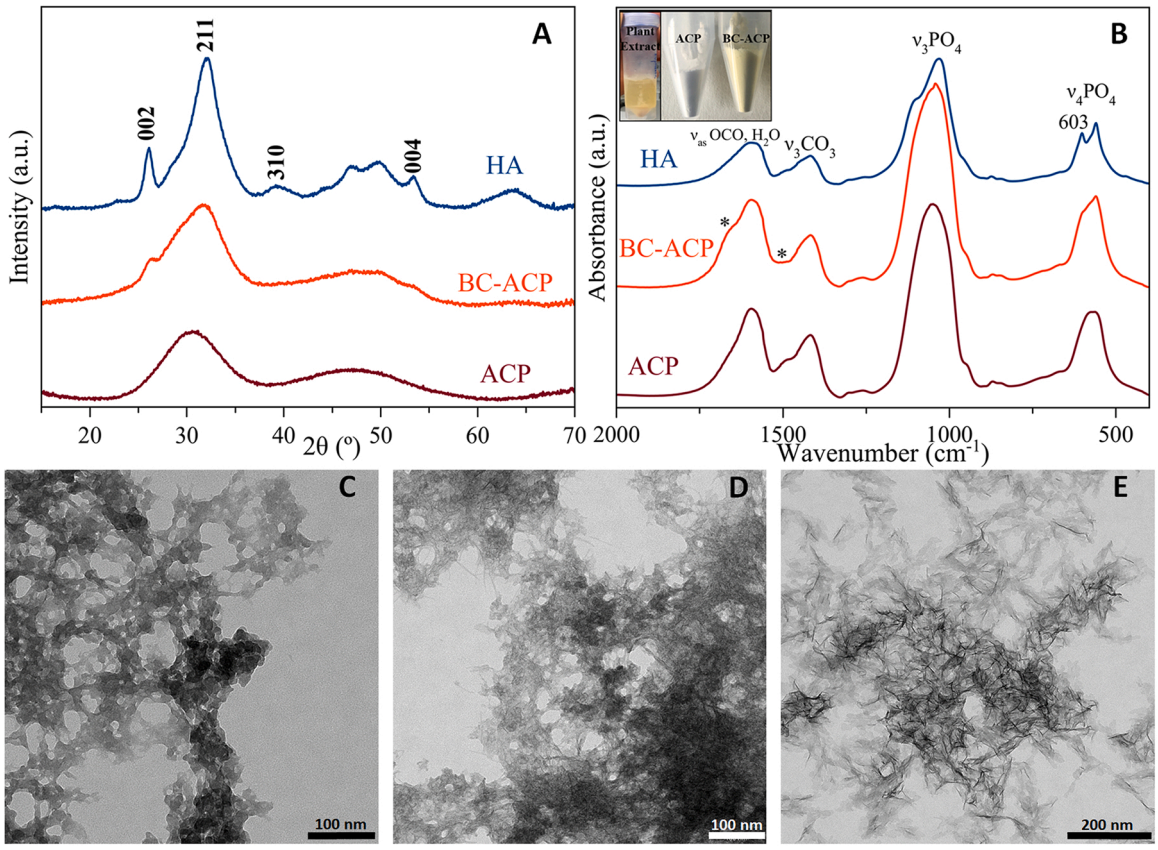

Fig. 2. XRD diffractograms (A) of ACP NPs (red line), BC-ACP (orange line) and blank control sample (HA, blue line). FTIR Spectra (B) of ACP (red line), BC-ACP (orange line) and crystalline HA (blue line). The inset shows a photograph of the plant extract and powdered ACP and BC-ACP samples. TEM images of (C) ACP, (D) BC-ACP and (E) blank HA. Insets show a region of each image at double magnification.

isolation. To preserve this content until its use, it was kept in liquid nitrogen. The extraction was carried out with QIAamp® PowerFecal® DNA kit following the manufacturer's protocol for process automation with the QIAcube robot. Quantification of gDNA was performed by fluorometry (qubit). gDNA samples were analyzed by sequencing the V4 region (233 bp) of 16S ribosomal RNA (rRNA) genes using the MiSeq system (Illumina, San Diego, CA, USA). Library preparation, pooling, and miniSeq sequencing were performed at the Institute of Parasitology and Biomedicine "López-Neyra" (IPBLN) from the Spanish National Research Council (CSIC). Reaction steps were as follows: denaturation 3 min at 95 °C, (denaturation 30 s at 95 °C, annealing 30 s at 55 °C, elongation 30 s at 72 °C) x 25 cycles, and extension 5 min at 72 °C indexed with 8 PCR cycles to amplify the V3-V4 regions of the 16S rRNA gene with the following primers: 16S ProV3V4 forward 5′-> 3′ 5′ CCTACGGGNBGCASCAG 3′ and 16S ProV3V4 reverse 5′-> 3′ 5′ GACTACNVGGGTATCTAATCC 3′. Results were obtained from the Illumina analysis software version 2.6.2.3 and presented for the taxonomic levels of Phylum, Family and Genus according to the top 8 or 9 for each taxonomic level.

2.17. RNA extraction and quantitative RT-qPCR of colon gene expression

To carry out RNA extraction, a portion of colon was homogenized in 1 ml of Tri-Reagent Total (Sigma-Aldrich). After solubilizing RNA in Rnase-free H_2O and treated with DNase (Applied Biosystems), 100–250 ng of RNA was reverse-transcribed according to standard protocols using a Lifepro Thermal Cycler (Bioer Serves Life, China). Quantitative RT-PCR was performed with QuantStudio 12 K Flex Real-Time PCR System (Applied Biosystems) using primer/probes for genes involved in oxidative metabolism (Nfe2l2, sod1, sod2, cat, gpx2), genes coding for detoxification pathways (NQO1 and gsta2), markers involved in inflammatory processes (Tnf, IL-1b y IL-6) and glucose metabolism (gcg) (Applied Biosystems). The PCR master mix reaction included the first-strand cDNA template, primers/probes, and 2X TaqMan Fast Universal PCR Master Mix, No AmpErase UNG (Applied Biosystems). Relative quantification was performed using the comparative Ct ($2^{-\Delta Ct}$) method. ß-actin was used as internal control.

2.18. Statistical Analyses

The results exposed were carried out through three independent experiments and data were expressed as mean ± SD. For group comparison, bivariate analyses, including Student's t-test and one-way ANOVA were applied. Statistical analyses were performed with Statistical Package for the Social Sciences (SPSS) v. 15.0. Differences were considered statistically significant at a p-value < 0.05.

3. Results and discussion

3.1. Synthesis of nanoparticles and functionalization with bioactive compounds

A simple precipitation batch method was used to obtain ACP NPs [47]. The XRD pattern of ACP (i.e., naked nanoparticles) revealed the lack of long-range periodicity, characteristic of (non-crystalline) amorphous phases (Fig. 2A, red line). After the adsorption of bioactive species from the extract, very tiny features related to the formation of nanocrystalline apatite (Ap) can be distinguished (Fig. 2A, orange line), indicating that the conversion from ACP to Ap started during the adsorption. On the contrary, the blank control sample (HA) showed very similar XRD patterns of nanocrystalline hydroxyapatite phase [11,48]. These findings indicated that the adsorption of BC inhibited (or slowed

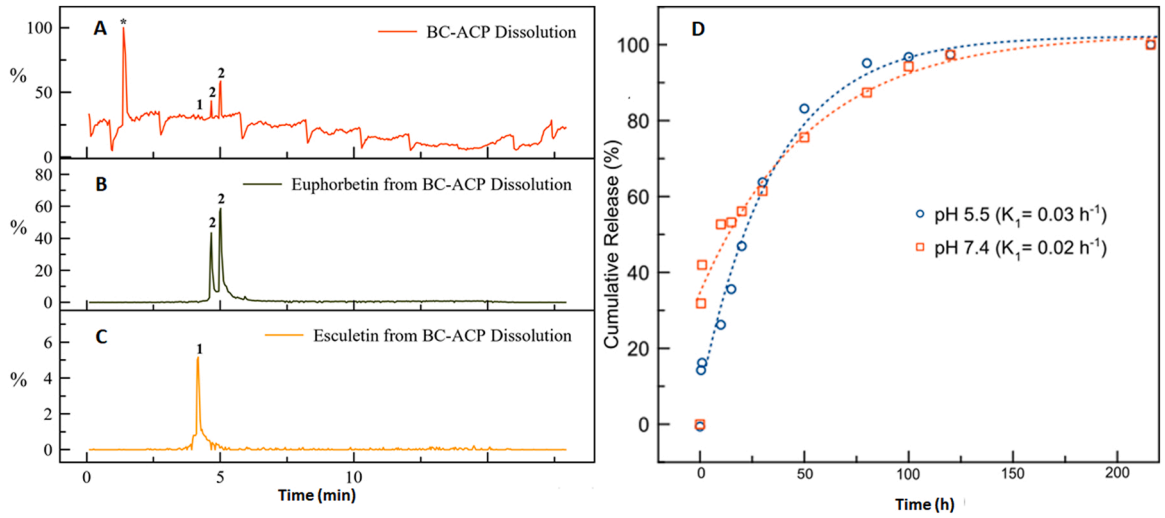

Fig. 3. UPLC-ESI-MS total ion current chromatogram in the negative ion mode from the decomposition of BC-ACP: (A) decomposition of BC-ACP and retention times corresponding to molecular weight of (B) euphorbetin and (C) esculetin,. 1 = esculetin; 2 = euphorbetin. (D) BC release profiles from amorphous BC-ACP in Potassium Phosphate Buffer pH 7.4 (empty squares) and in Sodium Citrate Buffer pH 5.5 (empty circles) during 9 days. The experimental data were fitted by first order kinetic models to obtain the theoretical release curves represented by dashed lines (release constants, K_1, are shown between brackets).

Table 1
Loading capacity and adsorption efficiency of the two coumarin derivates.

Compound	LC (mg g^{-1})	AE (%)
Esculetin	0.3 ± 0.0965	2.6 ± 1.2
Euphorbetin	3.4 ± 0.9	33.5 ± 17.2

down) the amorphous-to-crystalline conversion [49,50].

Fig. 2B represents the FTIR spectra of ACP, BC-ACP and HA samples. FTIR spectrum of ACP (in red) displays broad bands characteristic of the amorphous phase [51,52]. On the other hand, the FTIR spectrum of HA (in blue) confirms the presence of nano-crystalline apatite. Interestingly, BC-ACP FTIR spectrum (in orange) displays two absorption bands (marked with *) that can be associated to the functional groups C═C aromatic and C═C alkene of the adsorbed bioactive compounds on nanoparticles surface [53]. The change of the nanoparticles colour from white (ACP) to yellowish (BC-ACP) (inset of Fig. 2B) –yellowish, being similar to the plant extract colour- confirms the effective adsorption.

TEM images supported the FTIR and XRD results. TEM images of ACP (Fig. 2C) revealed aggregates of round-shaped amorphous NPs. On the other hand, HA sample showed thin needle-like NPs elongated along c-axis with the highest degree of crystallinity of all samples (Fig. 2E). Gradual transformation of amorphous phase of ACP to crystalline apatite composites in aqueous medium has been previously reported [50]. BC-ACP appeared to be a mixture of morphologies since TEM images revealed aggregates of amorphous round-shaped NPs and needle-like NPs with diffuse borders according to the XRD pattern (Fig. 2D).

The Ca/P ratio estimated by ICP for the ACP NPs was 1.67. However, for the BC-ACP and HA samples were slightly lower, 1.56 and 1.58, respectively. Decrease of Ca/P ratio is justified by typical release of calcium ions from ACP NPs during the adsorption of bioactive compounds. The Ca/P ratios for the NPs are shown in Additional file 1: Table S1.

3.2. Bioactive compounds adsorption on nanoparticles and release kinetics

Mass spectrometry characterization of the native *Euphorbia* extract and its bioactive compounds is described in Additional file 1: in section S1 (including Fig. S1 and Table S2). To identify and quantify the concentration of adsorbed bioactive compounds on NPs surface, BC-ACP were dissolved in acidic solution to induce the complete release of adsorbed molecules. Fig. 3A shows UPLC-ESI(-)-MS total ion current chromatogram of the species in solution after BC-ACP dissolution. The mayor peak at 1.378 min (labelled as *) corresponds to the molecular weigh of citrate. The adsorption of citrate on ACP is well reported [11]. Indeed, citrate molecules are naturally bounded to apatite in bones [54]. The retention times of 4.174 min and of 4.665 and 5.014 min corresponds to the molecular weight of esculetin and euphorbetin, respectively. The peaks of euphorbetin (labelled as 2 in Fig. 3A) are much more intense than the peak of esculetin (labelled as 1 in Fig. 3A), indicating a much higher surface concentration of euphorbetin.

Quantitative analysis of the two coumarins from *Euphorbia* extract adsorbed on BC-ACP was accomplished by UPLC-DAD. Loading capacity (LC) represents the bioactive molecules adsorbed per unit mass of NPs (mg g^{-1}) and adsorption efficiency (AE) indicates the functionalization yield (%). LC and AE results are listed in Table 1. LC were 0.3 mg of esculetin and 3.4 mg of euphorbetin per gram of BC-ACP NPs. This is in line with the intensity ratio of the peaks of esculetin and euphorbetin of Fig. 3A. We estimated that AE reached values of 2.6% and 33.5% for esculetin and euphorbetin, respectively.

The pH effect on BC release kinetic was analyzed to assess the use of BC-ACP as a controlled drug delivery system, since pH-dependent dissolution of BC-ACP can result in different release profiles depending on the pH of the media. Thus, we evaluated BC release kinetic at a pH of 7.4 (simulating the pH of blood) and at a more acidic pH of 5.5, simulating the slightly acidic tumor microenvironment and/or the pH inside cell lysosomes. Fig. 3D displays the time-dependent BC release from BC-ACP NPs, during 9 days. The initial burst effect can be due to desorption of weakly bound BC at the ACP surface. For both pH conditions, BC then follows a gradual and slow-release profile, which can be fitted to first order kinetics with release rates in the range 0.02 $h^{-1} < K_1 < 0.03\ h^{-1}$.

The experimental data were fitted to a first-order kinetic equation [50]. Calcium phosphate exhibit a pH-dependent solubility, i.e., the lower the pH, the higher is the solubility. This behavior can explain the slightly higher release at the more acidic pH 5.5 (K_1(pH 5.5) = 0.03 h^{-1}; K_1(pH 7.4) = 0.02 h^{-1}). These kinetics profiles are in agreement with the constants of NPs dissolution [50]. This means that the adsorbed species are released upon the slow particle dissolution occurring in the aqueous media, slightly faster at more acidic pH 5.5.

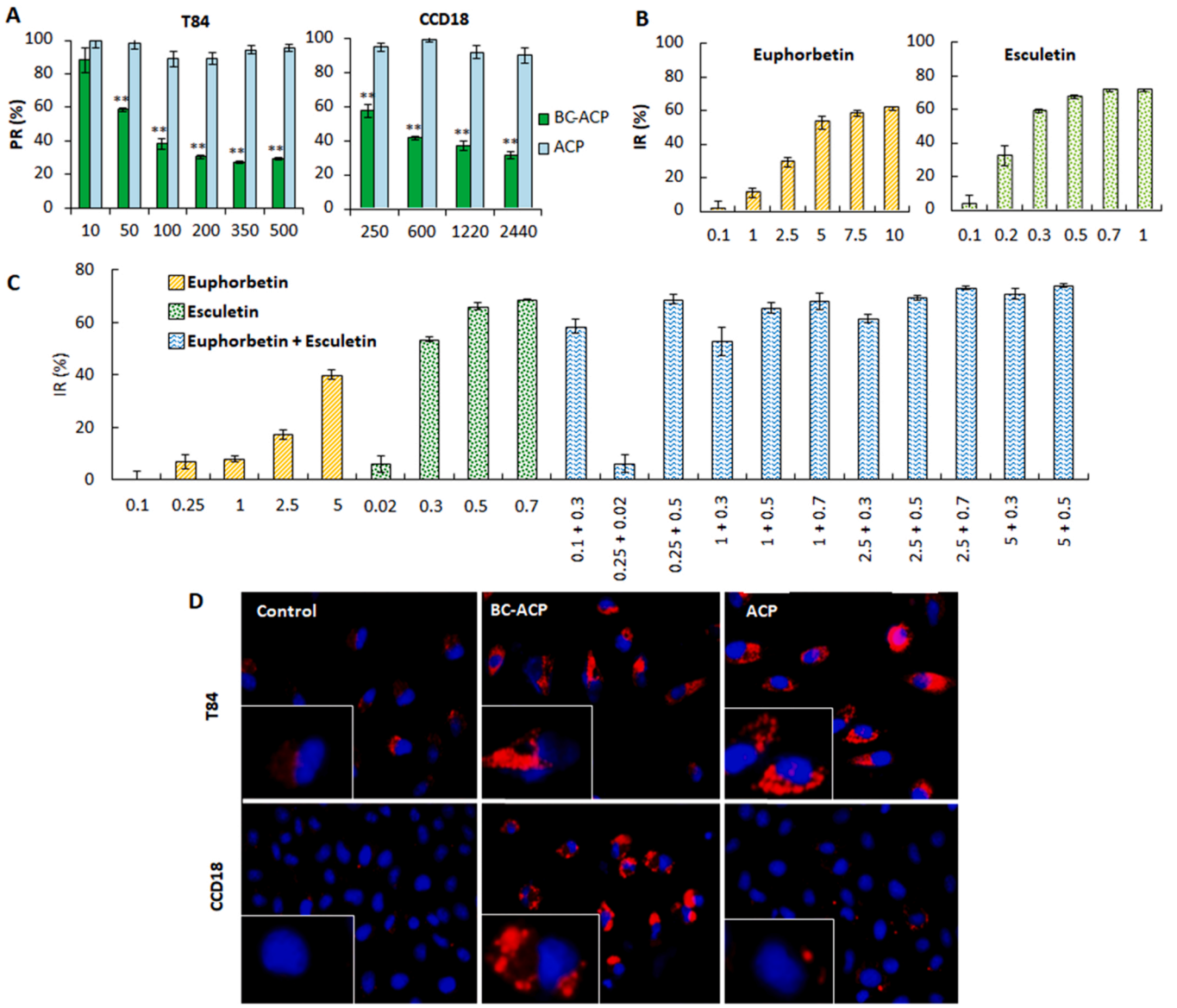

Fig. 4. Activity of BC and ACP in colon cell lines. (A) Antiproliferative activity of BC-ACP and ACP in colon cells. T84 and CCD18 cells were exposed to nanoparticles at different concentrations (μg nanoparticle/ml) for 72 h to obtain the IC_{50} values. (B) Antiproliferative assays using the esculetin and euphorbetin compounds. T84 cells were exposed to esculetin and euphorbetin (μg /ml) for 72 h in order to determine the IC_{50} values. (C) Antiproliferative assay of the combination of esculetin and euphorbetin. T84 cells were exposed to different esculetin and euphorbetin combinations (μg /ml) for 72 h in order to determine the IC_{50} values and synergic effect when they are combined. (D) A Lysotracker assay was carried out to analyze the internalization of nanoparticles. Data are presented as mean ± standard deviation of three independent experiments; *P < 0.05 relative to the respective control group. * *P < 0.01 relative to the respective control group.

After 9 days of release, the remaining (non-dissolved) nanoparticles at both pHs (pH 5.5 and pH 7.4) were decomposed and analyzed by UPLC-ESI(-)-MS in order to demonstrate that the complete release of BC from BC-ACP was achieved. Chromatograms (Additional file 1: Fig. S2) revealed no retention time signal for esculetin or euphorbetin, ensuring that the complete desorption of the compounds occurred after 9 days.

3.3. *Effect of nanoparticles, esculetin and euphorbetin on the viability of colon cells*

The NPs were assayed in CRC and non-tumor cells. As shown in Fig. 4A, ACP NPs did not induce toxicity in the T84 or CCD18 cell lines. In contrast, BC-ACP NPs showed a strong antitumor effect in the T84 cell line with an IC_{50} of 71.42 μg/ml whereas the IC_{50} in the non-tumor cell line CCD18 was 420.77 μg/ml, indicating a significant and selective cytotoxicity of BC-ACP against CRC cells. This selectivity had already been observed with the use of the native extract [31] and strongly suggests that the antitumor effect of BC-ACP was related to the presence of both esculetin and euphorbetin on the NP. In fact, esculetin showed a significant antitumor activity against some types of cancer, including CRC [34,55,56]. Conversely, euphorbetin has been scarcely studied as an antitumor agent.

To compare the antitumor activity of the NP with esculetin and euphorbetin, single molecules and combinations of esculetin/euphorbetinin were tested (Fig. 4B-C). IC_{50} values indicated higher antiproliferative activity of esculetin (0.27 μg/ml) in comparison to euphorbetin (4.69 μg/ml) (Fig. 4B). Combinations of both molecules were also tested using doses below the IC_{50}. As shown in Fig. 4C, the combination of euphorbetin/esculetin at the same concentration ratio of the extract (0.3/0.1 μg/ml) did not modulate the IC_{50} value. In contrast, the euphorbetin/esculetin concentration ratio found on the NPs (0.25/0.02 μg/ml) inhibited a very low percentage (10%) of cell proliferation.

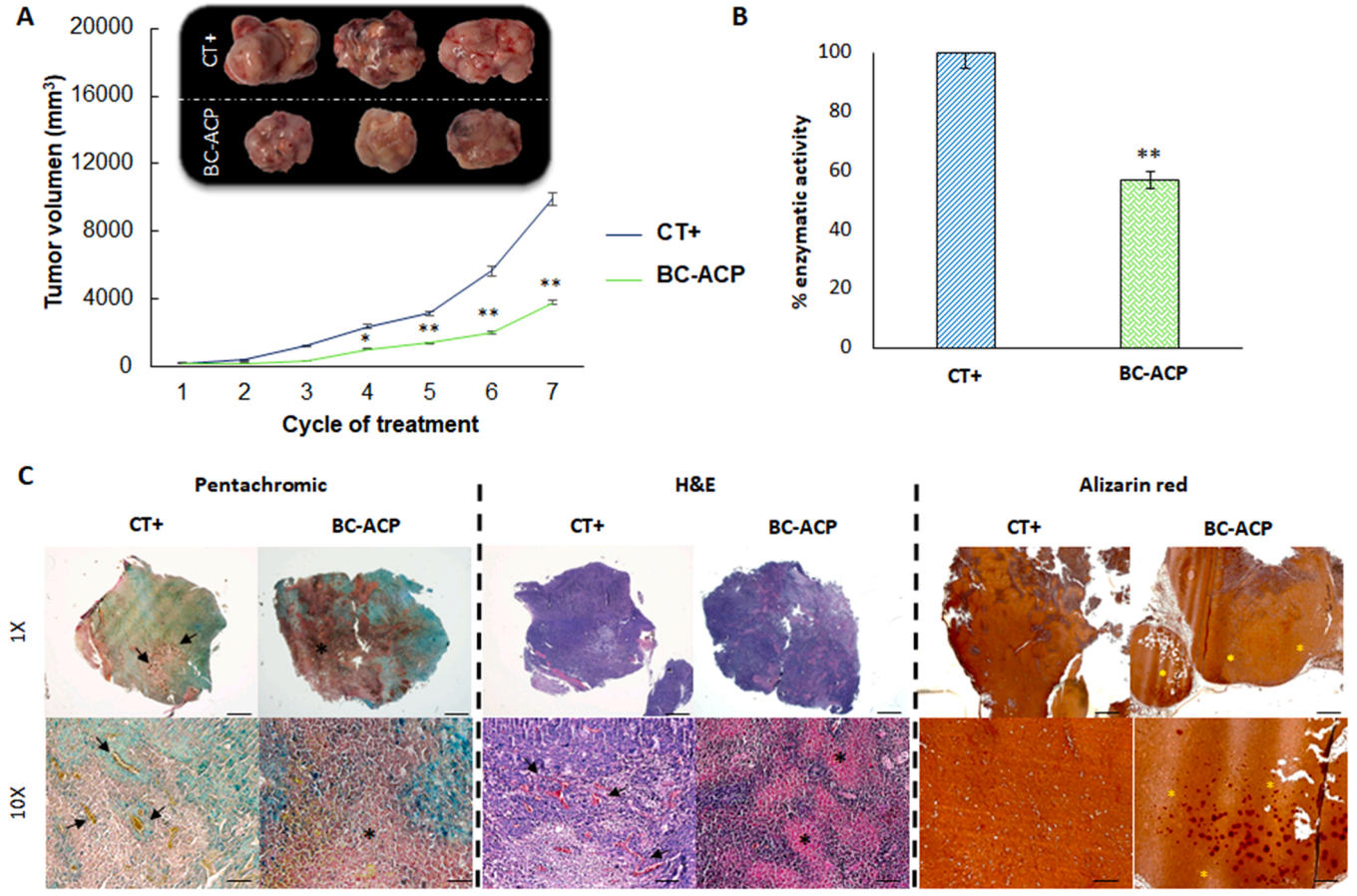

Fig. 5. *In vivo* antitumo activity of BC-ACP in CRC (subcutaneous induction). (A) Graphical representation of tumor volume (mm^3) during treatment with BC-ACP (7 cycles) and untreated mice (CT+) and representative images of tumors belonging to the CT+ and BC-ACP groups after the end point of the experiment and after euthanasia of the mice. Data are presented as mean ± standard deviation (n = 14). * * Significant inhibition of tumor growth comparing treatment with control ($p < 0.01$). (B) Graphical representation of carbonic anhydrase activity (percentage) measured in tumor samples belonging to the CT+ groups and treated with BC-ACP. Data are presented as mean ± standard deviation. * Significant inhibition of tumor growth comparing treatments with control ($p < 0.05$). (C) Histological analysis of subcutaneous tumor samples. Representative images of pentachrome, hematoxylin-eosin and alizarin red staining of tumor samples from CT+ and BC-ACP groups. Black asterisks indicate necrotic gaps, yellow asterisks show aggregated nanoparticles, and arrows indicate blood vessels. Scale bar = 100 μm.

These results suggest that the use of the NP associated with euphorbetin/esculetin represented a very remarkable advantage of antitumor action relative to the extract and/or the isolated molecules.

On the other hand, to demonstrate the internalization of NPs in cells (vesicle formation), a lysotracker assay was carried out. Previous results demonstrated that the native extract of *Euphorbia lathyris* induced autophagic vesicles and that esculetin induced autophagic death [31, 57]. As shown in Fig. 4D, both T84 and CCD18 cells exposed to high doses of BC-ACP showed vesicles. On the other hand, high doses of ACP induced a large number of internalizing vesicles in T84 tumor cells, but not in CCD18 cells, in which a low number of vesicles was detected. This finding could indicate that tumor cells have more hyperfunctional endocytosis mechanisms than normal cells, which would explain the low internalization of ACP NPs in normal cells (CCD18) compared to tumor cells (T84). This increase in endocytosis of ACP NPs could represent a mechanism of selective action against tumor cells.

3.4. Hemocompatibility of nanoparticles

A hemolysis assay using human erythrocytes was performed to evaluate the blood cell toxicity of BC-ACP. As shown in Additional file 1: Fig. S3A and B, neither BC-ACP nor ACP modified the morphology or agglutination of erythrocytes. A very low level of hemolysis (approximately 2%) was detected at doses of 122 μg/ml, indicating hemocompatibility [58]. In addition, a toxicity assay on white cells showed total absence of toxicity (viability around 100%) after 1 h and 12 h of exposure at all doses tested (Additional file 1: Fig. S3C).

3.5. BC-ACP inhibits CRC subcutaneous tumor growth

To determine the antitumor activity of BC-ACP, subcutaneous tumors were induced in mice by inoculation of MC-38 cells. As shown in Fig. 5A, treatment with BC-ACP (7 cycles) induced a significant reduction in tumor volume (62%) relative to the control group, detectable from the third treatment cycle onward.

3.5.1. BC-ACP reduces the activity of carbonic anhydrase in CRC subcutaneous tumors

Analysis of carbonic anhydrase in tumors treated with BC-ACP revealed a significant activity reduction (43.09%) relative to control mice (Fig. 5B). These results suggest that the antitumor effect of BC-ACP is closely related to the esculetin molecules present in the nanoformulations. According to Benej et al. and Na et al. [59,60], this polyphenol, which is an inhibitor of carbonic anhydrase IX, is characteristic of tumor tissues. This mechanism of antitumor activity, different from those of traditional chemotherapy, would be related to the loss of homeostasis in an acidic tumor environment. Indeed, the presence of large areas of tumor necrosis and fibrosis in tumor samples from mice treated with BC-ACP (as shown with H&E and pentachrome staining in Fig. 5C) could indicate an autophagy phenomenon similar to those

Table 2
Hemogram of CT+ and BC-ACP groups at the end of treatment.

Parameters	CT+	BC-ACP
WBC (10^3/μl)	11.15 ± 0.50	12.29 ± 1.05
RBC (10^6/μl)	4.78 ± 0.11	5.26 ± 0.18
HGB (g/dL)	8.17 ± 0.17	8.77 ± 0.3
HCT	24.81 ± 0.48	26.4 ± 0.86
PLT (10^3/μl)	700.64 ± 88.66	292.75 ± 10.29
LYM%	90.23 ± 0.36	91.42 ± 0.21
MON%	3.97 ± 0.14	3.09 ± 0.13
NEU%	4.10 ± 0.24	3.63 ± 0.12
EOS%	0.03 ± 0.00	0.04 ± 0.00
BAS%	1.67 ± 0.02	1.93 ± 0.07
MCV (fL)	52.51 ± 0.39	51.45 ± 0.41
MCH (pg)	17.24 ± 0.09	16.73 ± 0.07
RDW	17.55 ± 0.22	18.47 ± 0.33
MPV (fL)	8.24 ± 0.09	7.58 ± 0.04
PCT	0.12 ± 0.01	0.22 ± 0.00
PDW	30.91 ± 0.36	26.86 ± 0.43

WBC = Total number of white blood cells; LYM% = % of Lymphocytes; MON% = % of Monocytes / Macrophages; NEU% = % of Neutrophils / Polymorphonuclear leukocytes; EOS% = % of Eosinophils; BAS% = % of Basophils; RBC = Total number of red blood cells; HGB = Hemoglobin; HCT = % Volume of blood occupied by red blood cells (hematocrit); PLT = Total number of platelets; MCV = mean corpuscular volume; MCH = Mean corpuscular hemoglobin; RDW = Red blood cell distribution width; MPV = Mean platelet volume; PCT = % Volume of blood occupied by platelets (thrombocrit); PDW = Platelet size distribution. Data are presented as mean ± standard deviation.

Table 3
Hemogram from CT-, CT+ and BC-ACP groups before the end of the experiment.

Parameters	CT-	CT+	BC-ACP
WBC (10^3/μl)	9.86 ± 1.00	6.97 ± 0.94	7.29 ± 1.29
RBC (10^6/μl)	10.22 ± 0.88	7.89 ± 1.31	8.41 ± 0.9
HGB (g/dL)	16.08 ± 1.31	12.6 ± 1.13	13.22 ± 1.16
HCT	46.43 ± 3.79	38.32 ± 2.80	29.56 ± 3.32
PLT (10^3/μl)	672.44 ± 97.01	430.92 ± 54.33	650.5 ± 224.75
LYM%	95.13 ± 0.95	93.04 ± 1.28	94.52 ± 0.85
MON%	0.39 ± 0.06	0.94 ± 0.07	0.68 ± 0.22
NEU%	3.81 ± 1.02	4.83 ± 0.09	3.5 ± 0.44
EOS%	0.24 ± 0.05	0.1 ± 0.00	0.04 ± 0.00
BAS%	0.44 ± 0.16	1.08 ± 0.26	1.26 ± 0.35
MCV (fL)	45.49 ± 1.46	48.93 ± 4.63	47.09 ± 1.06
MCH (pg)	15.77 ± 0.46	16.11 ± 1.21	15.75 ± 0.31
RDW	14.01 ± 0.50	16.41 ± 2.34	16.87 ± 1.53
MPV (fL)	5.88 ± 0.07	7.88 ± 0.81	6.94 ± 0.87
PCT	0.43 ± 0.11	0.19 ± 0.13	0.44 ± 0.07
PDW	22.3 ± 3.26	35.3 ± 8.91	24.62 ± 4.48

WBC = Total number of white blood cells; LYM% = % of Lymphocytes; MON% = % of Monocytes / Macrophages; NEU% = % of Neutrophils / Polymorphonuclear leukocytes; EOS% = % of Eosinophils; BAS% = % of Basophils; RBC = Total number of red blood cells; HGB = Hemoglobin; HCT = % Volume of blood occupied by red blood cells (hematocrit); PLT = Total number of platelets; MCV = mean corpuscular volume; MCH = Mean corpuscular hemoglobin; RDW = Red blood cell distribution width; MPV = Mean platelet volume; PCT = % Volume of blood occupied by platelets (thrombocrit); PDW = Platelet size distribution. Data are presented as mean ± standard deviation.

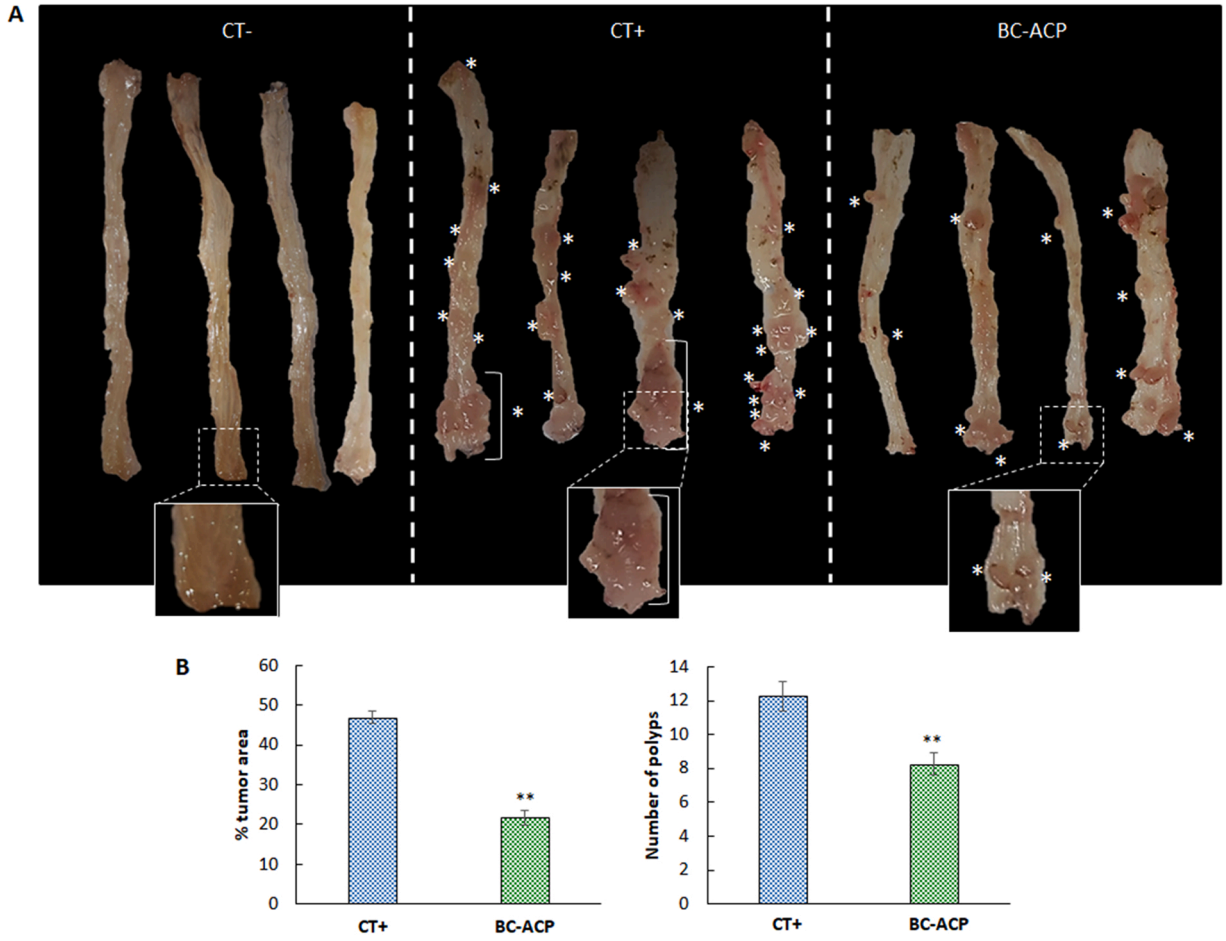

Fig. 6. *In vivo* treatment with BC-ACP using the AOM/DSS model of CRC. (A) Representative macroscopic images of dissected colon (four mice) after complete treatment with BC-ACP. Polyp formation is marked with asterisks. (B) Graphical representation of the number of polyps and percentage of tumor area in the colon of the groups treated with BC-ACP and the untreated group (CT+). Data are presented as mean ± standard deviation (n = 14). (**) Significant inhibition of tumor growth, treatment vs control ($p < 0.01$).

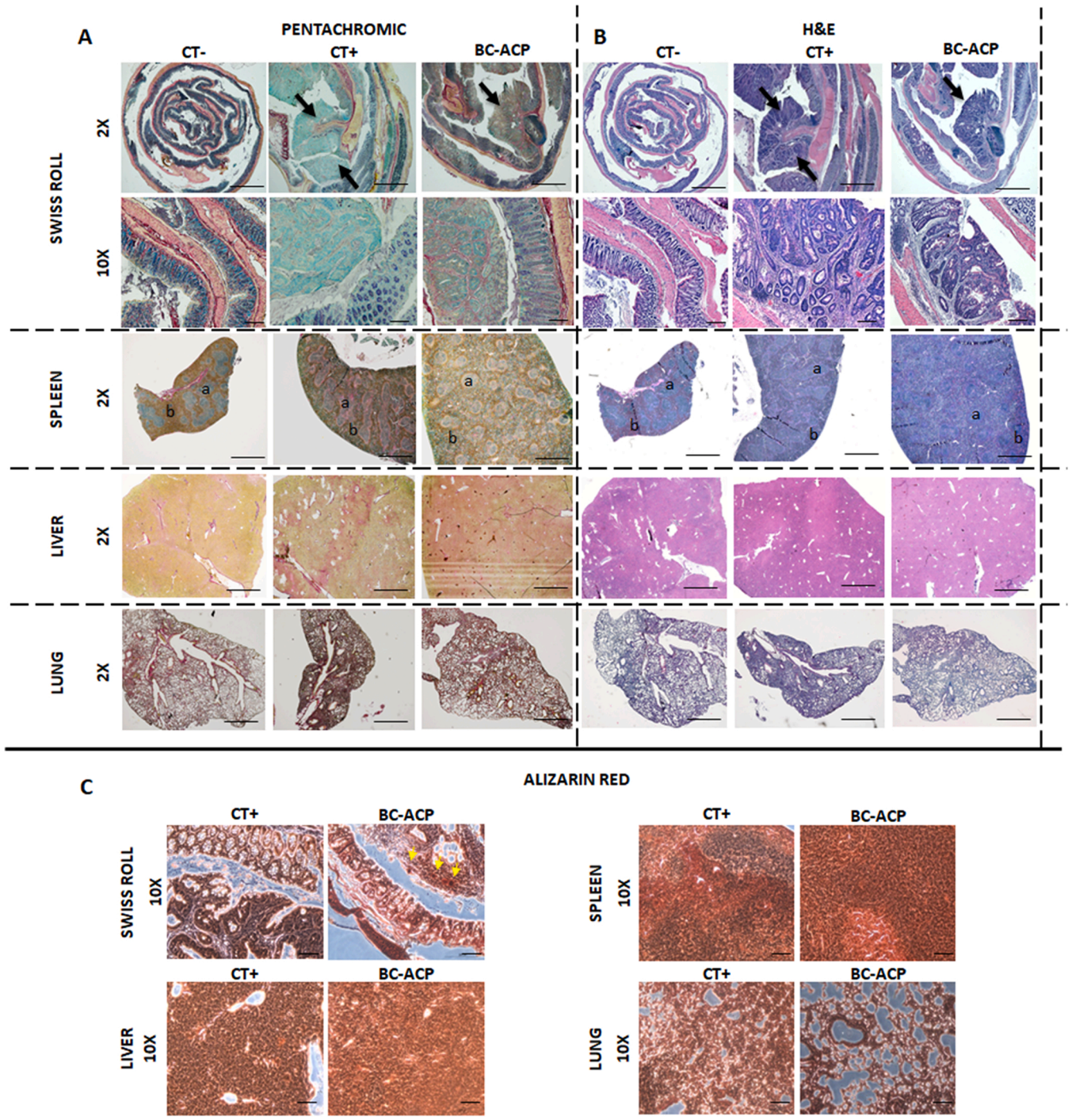

Fig. 7. Histological analysis of tumors after treatment with BC-ACP. (A) Pentachrome staining and (B) H&E staining of colon (Swiss roll), spleen, liver and lung samples. The Swiss roll technique was used to analyze treated (BC-ACP), untreated (CT+) and control (CT-) groups. Pentachrome staining shows dysplastic polyps as green structures without globet cells (violet, black arrows) and with some collagen tracts (red arrows). H&E staining shows polyps with dysplasia (black arrows). Spleen samples with white pulp (a) and red pulp (b). Regarding CT+ samples, invasion of white pulp into red pulp was observed. Liver samples showed fibrotic tracts (collagen, red) in the CT+ group that were not seen in the BC-ACP and CT- groups. Lung samples from the CT+ group showed fibrotic changes (green arrows) not present in the BC-ACP and CT- groups. (C) Representative images of alizarin red staining of tumor samples from the CT+ and BC-ACP groups. Accumulations of BC-ACP can be observed in colon samples (yellow arrows).

observed in vitro. This phenomenon could be mediated by esculetin through disturbance of acid-base balance homeostasis.

3.5.2. *Histological analysis of CRC subcutaneous tumor samples*

Tumor samples were fixed and treated for histological analysis using H&E, pentachrome, and alizarin red methods. As shown in Fig. 5C, pentachrome images revealed the absence of vasculature and red blood cells (yellow) in tumors treated with BC-ACP relative to controls, as well as an enriched collagen matrix (red). H&E images showed less nuclear staining and cellular debris due to cell apoptosis (black asterisks). In addition, alizarin red staining evidenced aggregations of NPs (red), demonstrating the accumulation and selective localization of BC-ACP in the subcutaneous tumor. This finding may be related to the well-known EPR (enhanced permeability and retention) phenomenon, according to

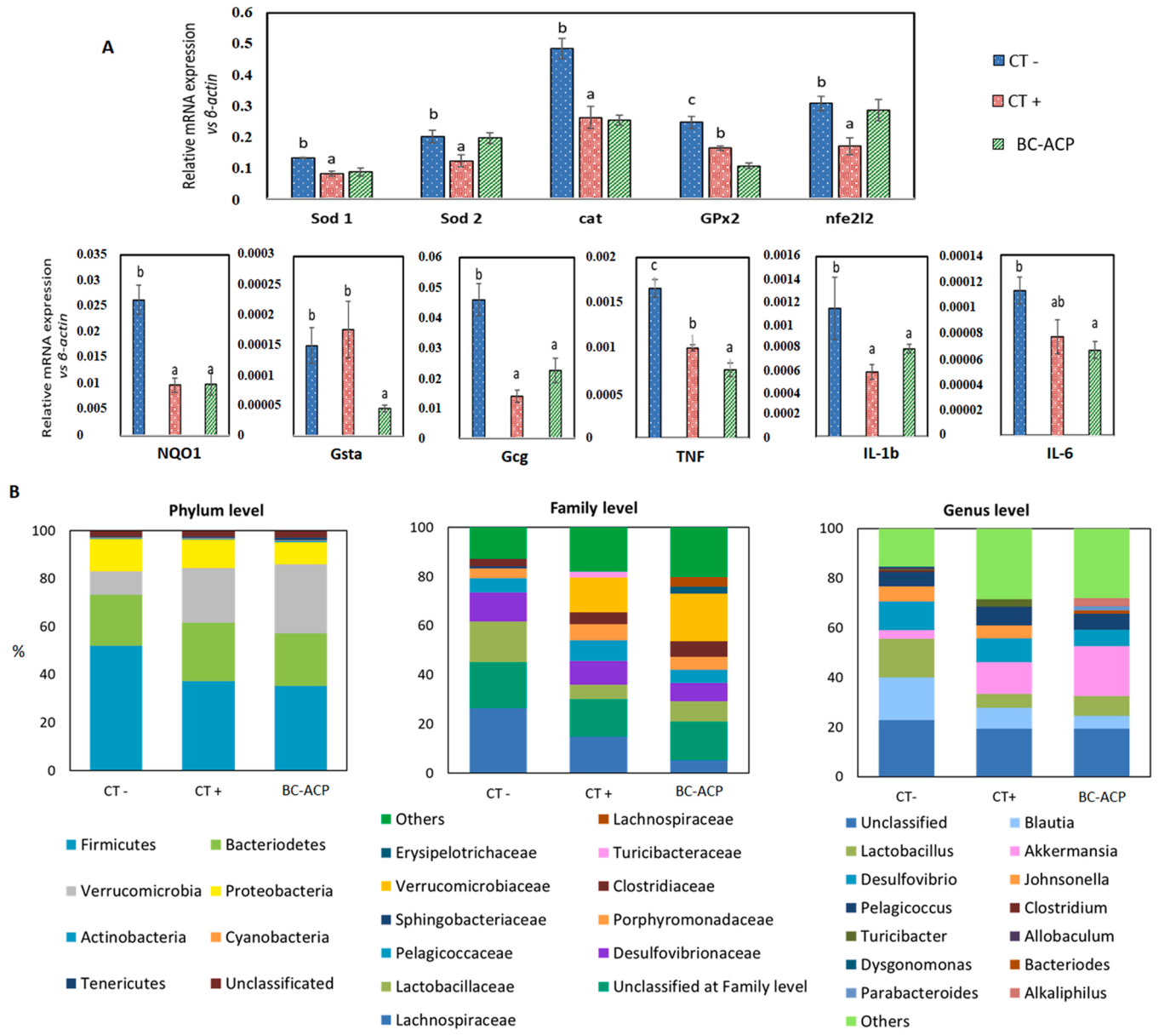

Fig. 8. Oxidative stress system, inflammatory cytokines and microbiome analysis after treatment with BC-ACP. (A) Graphical representation of inflammatory cytokines (TNF-alpha, IL-6 and IL-1b) and oxidative stress enzymes (SOD1, SOD2, CAT, GPX2, NFE2L2, NQO1, GSTA and GCG) expression in colon samples after treatment with BC-ACP compared to the untreated group. Bars with different letters (a,b,c) denote significant differences ($p < 0.05$) among experimental groups. (B) Graphical representation of the percentage of different bacteria at the phylum, family and genus levels in colon samples from CT-, CT+ and BC-ACP groups. Data represent the mean values of triplicate samples.

which the leaky vasculature of the tumor would allow nanoformulations to be retained in tumor tissues but not in healthy ones. In fact, the selective accumulation of calcium phosphate NPs carrying doxorubicin in breast cancer tissues has been previously observed [61].

3.5.3. *Hematological analysis after treatment with BC-ACP*

The blood of the mice was subsequently analyzed to determine the impact of the BC-ACP treatment in the hematological parameters. The results showed no significant abnormalities, indicating null toxicity of BC-ACP (Table 2). It should be noted that the values of WBC, HGB and PLT were significantly lower than those observed in mice treated with the native extract [62].

3.6. *BC-ACP reduces polyps size and number in CRC induced by AOM/DSS*

Further experiments on a different CRC model induced by AOM/DSS in C57BL/6 mice confirmed the antitumor activity of BC-ACP. As shown in Fig. 6A, macroscopic analysis revealed a significant decrease in the number and size of polyps in the group treated with BC-ACP. In addition, the tumor area was reduced to below 25%, around the half of the tumor area observed in the untreated group (ca. 50%, Fig. 6B).

3.6.1. *Hematological analysis after treatment with BC-ACP*

As in the subcutaneous CRC model, treatment with BC-ACP showed no toxicity in any of the hematological parameters analyzed (Table 3).

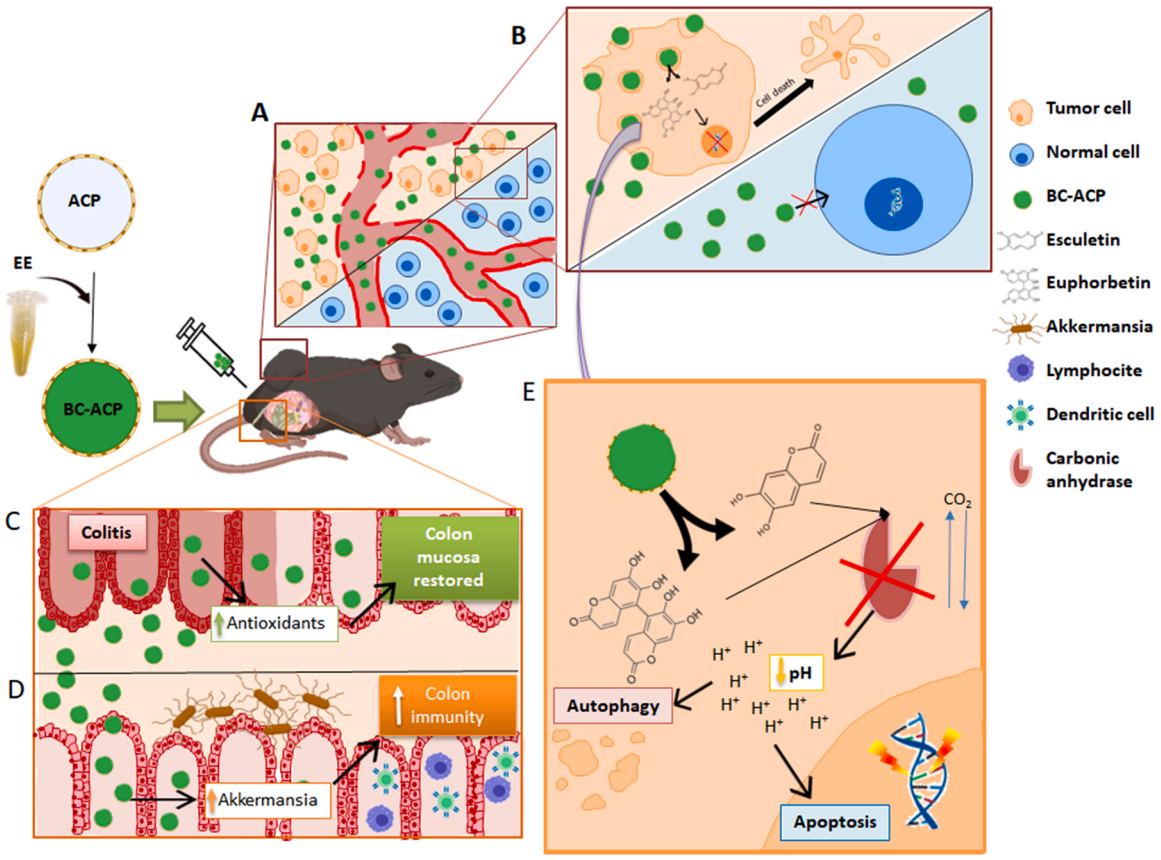

Fig. 9. . Schematic representation of the model of antitumor activity of BC-ACP according to the results obtained. (A) EPR phenomenon and selective accumulation of BC-ACP in cancer tissues (orange) with respect to normal tissues (blue). (B) Increased endocytosis in cancer cells with respect to normal cells. (C) Effect of BC-ACP in the colonic mucosa, consisting of antioxidant effect of esculetin and euphorbetin that reverts inflammation in the colonic mucosa and (D) increases *Akkermansia* colonization and colonic immunity. (E) Euphorbetin and esculetin present in BC-ACP nanoparticles inhibit carbonic anhydrase in tumors, decreasing intracellular pH and leading to cell death, mainly by autophagy but also by apoptotic pathways.

3.6.2. Histological analysis of CRC induced by AOM / DSS after BC-ACP treatment

As shown in Fig. 7A and B, microscopic analyses (H&E and pentachrome methods) of Swiss roll colon samples showed an evident decrease in polyps with high-grade dysplasia in the colonic mucosa of mice treated with BC-ACP in comparison with untreated CT+ mice (controls). The dysplastic polyps were composed of colonic epithelial cells containing aberrant nuclei and their colonic crypt organization was abnormal with no globet cells. In addition, pentachrome staining of spleen samples showed a large invasion of white pulp (blue) into the red pulp (olive green) in CT+ . Both H&E and pentachrome staining of lung samples showed fibrosis in CT+ that was not observed in the BC-ACP group. Similarly, liver samples showed fibrotic changes on pentachrome staining (collagen, red) in CT+ but not in the BC-ACP group. Finally, as in subcutaneous tumors, alizarin red staining demonstrated uptake of BC-ACP in the colonic epithelium (Fig. 7C).

Thus, our results showed that BC-ACP nanoformulations reduce the development of polyps in the colonic mucosa of mice. Most likely, the euphorbetin and esculetin present in these nanoformulations act as antioxidants that decrease the damage caused by AOM/DSS during the induction of dysplastic colonic polyps [63]. In addition, the use of calcium phosphate NPs has been of great advantage in our colon cancer treatment strategy, in line with previous studies that reported good results using these NPs for cancer therapy in preclinical models. For instance, Luo et al. [64,65] used this nanocarrier in vitro to silence KRAS mutation in pancreatic cancer cell lines by transporting siRNAs with satisfactory results, and Ansari et al. [64,65] demonstrated increased antitumor activity of epirubicin using hydroxyapatite nanocarriers. In our case, the accumulation of BC-ACP nanoformulations in the colonic mucosa (alizarin red staining) but not in the liver or spleen (mononuclear phagocyte system) was highly positive. This fact suggested the prevention of BC-ACP sequestration in organs other than the colon, one of the great workhorses for the clinical application of nanoformulations [66,67].

3.6.3. Expression of oxidative stress systems and inflammatory cytokines

Colon samples were processed to analyze the modulation in the expression of oxidative stress detoxification systems by RT-qPCR. The CT+ group showed a significant decrease (approximately 50%) in the expression of most of the enzymes analyzed (except GSTA) relative to the healthy control group (CT-) (Fig. 8A). Interestingly, the BC-ACP group showed a significantly lower decrease in the expression of these enzymes (especially SOD2, GPX2 and NFE2L2) compared to the CT+ group (Fig. 8A). Moreover, the levels of pro-inflammatory cytokines (TNF-alpha, IL-6 and IL-1b) were significantly diminished in the CT+ samples. These changes were also found in the BC-ACP group, although, notably, the expression of IL-1b was higher than that observed in the untreated CT+ group. These results could help to explain the histological damage to the liver and lung in the CT+ group, in which a lower expression of the enzymes intended for protection against oxidative stress (SOD, GPx2, Nfe2l2 or NQO1) was detected. In contrast, a higher expression of these protective enzyme systems (especially SOD2, Nfe2l2 and Gcg) was observed in mice treated with BC-ACP.

3.6.4. Analysis of the microbiome

The family Clostridiaceae increased in CT+ compared to CT- and

significantly decreased after treatment with BC-ACP (Fig. 8B). In addition, the genus *Lactobacillus* predominated in the CT- group while decreased significantly in the CT+ group, with a predominance of colitogenic bacteria such as the genera *Akkermansia* (Verrucomicrobiaceae) and *Turicibacter*. Interestingly, after treatment with BC-ACP, the latter genus disappeared. Moreover, *Akkermansia* increased in the BC-ACP group compared to CT+ . This bacterium has been previously associated to an efficient response to immunotherapeutic treatments against cancer and a more effective immune response of the organism against tumor tissues [68,69]. Recently, Fuhren et al. demonstrated that calcium phosphate NPs could reduce the presence of *Akkermansia* in the colon [70]. However, BC-ACP did not inhibit the proliferation of this genus in the intestinal microbiota of mice, suggesting that the presence of polyphenols (esculetin and euphorbetin) in the nanoformulation could act as upregulators of *Akkermansia* and, therefore, be beneficial to prevent the appearance of dysplastic polyps and colon cancer. In summary, the results suggest the general model represented in Fig. 9 to explain the preventive and antitumor activity of BC-ACP against CRC.

4. Conclusions

We have successfully synthesized ACP NPs, following an easy and low-cost strategy that avoided the use of toxic chemicals and high pressures and temperatures. These NPs are capable of adsorbing on their surface biologically active compounds from a natural extract from plants of the family Euphorbiaceae. The efficiency of the adsorption process and loading capacity of BC-ACP were evaluated by UPLC-DAD measurements, which revealed a loading capacity of 3.4 mg euphorbetin and 0.3 mg esculetin adsorbed per gram of NPs. The adsorption efficiencies were approximately 33.5% and 2.6% for euphorbetin and esculetin, respectively. The release of BC from BC-ACP was time and pH-dependent, being slightly faster at lower pH values (5.5) than at pH 7.4 (0.03 h^{-1} and 0.02 h^{-1}, respectively), in agreement with the pH-dependent dissolution of ACP, favored at acidic pH values. Thus, BC-ACP NPs represent a suitable controlled drug delivery system for the treatment of CRC. Interestingly, these functionalized nanoparticles showed high antitumor activity against T84 colon cancer cells with an IC_{50} of 71.42 μg/ml whereas the IC_{50} in the non-tumor cell line CCD18 was 420.77 μg/ml, suggesting a selective effect on tumor cells from the colon. The combination of two bioactive compounds (esculetin and euphorbetin) on the NPs was essential to exert this antitumor effect. Therefore, these NPs represent an advantage over the use of both bioactive compounds independently. In addition, the NPs exhibited high hemocompatibility and did not affect the viability of erythrocytes or white blood cells. Furthermore, these NPs have a selective biodistribution to colonic and tumor tissues and are not found in the mononuclear phagocytic system (liver or spleen). Finally, BC-ACP NPs also demonstrated antioxidant and colonic immunostimulant properties, the latter related to the selection of *Akkermansia* in the intestinal microbiome. The efficacy of the NPs was demonstrated on two diferent in vivo CRC models: subcuatenous tumors and CRC induced by *AOM / DSS*. The treatment with BC-ACP significantly reduced the volume of the subcutaneous tumors (43.09%) and the tumor area in the colon (25%). The NPs also decreased dysplastic polyps in the colonic mucosa 33% with respect to the control group, suggesting a preventive effect. Overall, these results indicate that BC-ACP may be a new strategy to improve the treatment of CRC, being a very promising candidate for future human clinical trials.

Conflict of Interest

The authors declare no conflict of interest.

Data Availability

No data was used for the research described in the article.

Acknowledgements

This research was funded by the Spanish Ministry of Science, Innovation and Universities as well as the European Union (PTQ-17-09172, RTC-2017-6540-1, RTI2018-100934-B-I00, RTC2019-006870-1, RYC-2016-21042) and in part by Junta de Andalucía (P18-TP-1420, A-CTS-666-UGR20, B-CTS-122-UGR20, P18-HO-3882 and P18-TP-0969) FEDER program. In addition, this work was supported by funds from research groups AGR145, FQM-368 and CTS-107 (Andalusian Government). The authors would like to thank technical assistance from the Centro de Instrumentación Científica (CIC) (Granada University) and Antonio Murillo Cancho from the University of Almería and CELLBITEC S.L. All animal experiments were conducted under the Ethical and Regulatory Guidelines for Animal Experiments defined by the University of Granada (Certificate number: 16/01/2020/005).

CRediT authorship contribution statement

C. Mesas and V. Garcés contributed equally to this study on designing and performing the experiments. Conceptualization: J. Prados, J. M. Delgado-López and F. Bermúdez; Data curation: R. Martínez, R. Ortíz and K. Doello; Formal analysis: R. Martínez, R. Ortíz, K. Doello and M. Dominguez-Vera; Funding acquisition: J. Prados, J. M. Delgado-López, C. Melguizo, J. M. Porres, F. Bermúdez. Investigation and Methodology: C. Mesas, V. Garcés, R. Ortíz and K. Doello; Software: R. Martínez, M. Dominguez-Vera. Supervision: J. Prados, J. M. Delgado-López, C. Melguizo and J. M. Porres; Validation and Visualization: R. Martínez. Writing - original draft: C. Mesas and V. Garcés; Writing - review & editing: J. Prados, J. M. Delgado-López and C. Melguizo. All authors have read and agreed to the published version of the manuscript.

Appendix A. Supporting information

Supplementary data associated with this article can be found in the online version at doi:10.1016/j.biopha.2022.113723.

References

[1] R.L. Siegel, K.D. Miller, A. Jemal, Cancer statistics, 2018, CA Cancer J. Clin. 68 (2018) 7–30, https://doi.org/10.3322/caac.21442.
[2] The Lancet, GLOBOCAN 2018: counting the toll of cancer, Lancet 392 (2018) 985, https://doi.org/10.1016/S0140-6736(18)32252-9.
[3] E.J. Kuipers, W.M. Grady, D. Lieberman, T. Seufferlein, J.J. Sung, P.G. Boelens, C.J. H. Van De Velde, T. Watanabe, Colorectal cancer, Nat. Rev. Dis. Prim. 1 (2015) 1–25, https://doi.org/10.1038/nrdp.2015.65.
[4] A. Fernández Montes, N. Martínez Lago, M. Covela Rúa, J. de la Cámara Gómez, P. González Villaroel, J.C. Méndez Méndez, M. Jorge Fernández, M. Salgado Fernández, M. Reboredo López, G. Quintero Aldana, M. Luz Pellón Augusto, B. Graña Suárez, J. García Gómez, Efficacy and safety of FOLFIRI/aflibercept in second-line treatment of metastatic colorectal cancer in a real-world population: prognostic and predictive markers, Cancer Med 8 (2019) 882–889, https://doi.org/10.1002/cam4.1903.
[5] S.G. Klochkov, M.E. Neganova, V.N. Nikolenko, K. Chen, S.G. Somasundaram, C. E. Kirkland, G. Aliev, Implications of nanotechnology for the treatment of cancer: Recent advances, Semin. Cancer Biol. (2019) 0–1, https://doi.org/10.1016/j.semcancer.2019.08.028.
[6] F. Moradi Kashkooli, M. Soltani, M. Souri, Controlled anti-cancer drug release through advanced nano-drug delivery systems: Static and dynamic targeting strategies, J. Control. Release 327 (2020) 316–349, https://doi.org/10.1016/j.jconrel.2020.08.012.
[7] S. Hossen, M.K. Hossain, M.K. Basher, M.N.H. Mia, M.T. Rahman, M.J. Uddin, Smart nanocarrier-based drug delivery systems for cancer therapy and toxicity studies: a review, J. Adv. Res. 15 (2019) 1–18, https://doi.org/10.1016/j.jare.2018.06.005.
[8] J. Fang, H. Nakamura, H. Maeda, The EPR effect: unique features of tumor blood vessels for drug delivery, factors involved, and limitations and augmentation of the effect, Adv. Drug Deliv. Rev. 63 (2011) 136–151, https://doi.org/10.1016/J.ADDR.2010.04.009.
[9] H. Maeda, T. Sawa, T. Konno, Mechanism of tumor-targeted delivery of macromolecular drugs, including the EPR effect in solid tumor and clinical overview of the prototype polymeric drug SMANCS, J. Control. Release 74 (2001) 47–61, https://doi.org/10.1016/S0168-3659(01)00309-1.
[10] J. Prados, C. Melguizo, R. Ortiz, C. Velez, P.J. Alvarez, J.L. Arias, M.A. Ruiz, V. Gallardo, A. Aranega, Doxorubicin-loaded nanoparticles: new advances in breast

cancer therapy, Anticancer Agents Med. Chem. 12 (2012) 1058–1070, https://doi.org/10.2174/187152012803529646.
[11] J.M. Delgado-López, M. Iafisco, I. Rodríguez, A. Tampieri, M. Prat, J. Gómez-Morales, Crystallization of bioinspired citrate-functionalized nanoapatite with tailored carbonate content, Acta Biomater. 8 (2012) 3491–3499, https://doi.org/10.1016/j.actbio.2012.04.046.
[12] M. Iafisco, L. Degli Esposti, G.B. Ramírez-Rodríguez, F. Carella, J. Gómez-Morales, A.C. Ionescu, E. Brambilla, A. Tampieri, J.M. Delgado-López, Fluoride-doped amorphous calcium phosphate nanoparticles as a promising biomimetic material for dental remineralization, Sci. Rep. 8 (2018) 1–9, https://doi.org/10.1038/s41598-018-35258-x.
[13] C. Combes, C. Rey, Amorphous calcium phosphates: synthesis, properties and uses in biomaterials, Acta Biomater. 6 (2010) 3362–3378, https://doi.org/10.1016/j.actbio.2010.02.017.
[14] X. Li, H. Zeng, L. Teng, H. Chen, Comparative investigation on the crystal structure and cell behavior of rare-earth doped fluorescent apatite nanocrystals, Mater. Lett. 125 (2014) 78–81, https://doi.org/10.1016/j.matlet.2014.03.151.
[15] X. Li, J. Zhu, Z. Man, Y. Ao, H. Chen, Investigation on the structure and upconversion fluorescence of Yb3+/Ho3+ co-doped fluorapatite crystals for potential biomedical applications, Sci. Rep. 4 (2015) 4–10, https://doi.org/10.1038/srep04446.
[16] F. Oltolina, L. Gregoletto, D. Colangelo, J. Gómez-Morales, J.M. Delgado-López, M. Prat, Monoclonal antibody-targeted fluorescein-5-isothiocyanate-labeled biomimetic nanoapatites: a promising fluorescent probe for imaging applications, Langmuir 31 (2015) 1766–1775, https://doi.org/10.1021/la503747s.
[17] X. Guo, W. Li, H. Wang, Y.Y. Fan, H. Wang, X. Gao, B. Niu, X. Gong, Preparation, characterization, release and antioxidant activity of curcumin-loaded amorphous calcium phosphate nanoparticles, J. Non-Cryst. Solids 500 (2018) 317–325, https://doi.org/10.1016/j.jnoncrysol.2018.08.015.
[18] M. Iafisco, J.M. Delgado-Lopez, E.M. Varoni, A. Tampieri, L. Rimondini, J. Gomez-Morales, M. Prat, Cell surface receptor targeted biomimetic apatite nanocrystals for cancer therapy, Small 9 (2013) 3834–3844, https://doi.org/10.1002/smll.201202843.
[19] I. Rodríguez-Ruiz, J.M. Delgado-López, M.A. Durán-Olivencia, M. Iafisco, A. Tampieri, D. Colangelo, M. Prat, J. Gómez-Morales, PH-responsive delivery of doxorubicin from citrate-apatite nanocrystals with tailored carbonate content, Langmuir 29 (2013) 8213–8221, https://doi.org/10.1021/la4008334.
[20] (null) Neha Desai, M. Momin, T. Khan, S. Gharat, R.S. Ningthoujam, A. Omri, Metallic nanoparticles as drug delivery system for the treatment of cancer, Expert Opin. Drug Deliv. 18 (2021) 1261–1290, https://doi.org/10.1080/17425247.2021.1912008.
[21] H.M. Habib, C. Platat, E. Meudec, V. Cheynier, W.H. Ibrahim, Polyphenolic compounds in date fruit seed (Phoenix dactylifera): characterisation and quantification by using UPLC-DAD-ESI-MS, J. Sci. Food Agric. 94 (2014) 1084–1089, https://doi.org/10.1002/jsfa.6387.
[22] G. Kapravelou, R. Martínez, A.M. Andrade, C. Sánchez, C.L. Chaves, M. López-Jurado, P. Aranda, S. Cantarero, F. Arrebola, E. Fernández-Segura, M. Galisteo, J. M. Porres, Health promoting effects of Lupin (Lupinus albus var. multolupa) protein hydrolyzate and insoluble fiber in a diet-induced animal experimental model of hypercholesterolemia, Food Res. Int. 54 (2013) 1471–1481, https://doi.org/10.1016/j.foodres.2013.10.019.
[23] R. Martínez, G. Kapravelou, A. Donaire, C. Lopez-Chaves, F. Arrebola, M. Galisteo, S. Cantarero, P. Aranda, J.M. Porres, M. López-Jurado, Effects of a combined intervention with a lentil protein hydrolysate and a mixed training protocol on the lipid metabolism and hepatic markers of NAFLD in Zucker rats, Food Funct. 9 (2018) 830–850, https://doi.org/10.1039/c7fo01790a.
[24] I.A. Stringlis, R. De Jonge, C.M.J. Pieterse, The age of coumarins in plant-microbe interactions, Plant Cell Physiol. 60 (2019) 1405–1419, https://doi.org/10.1093/pcp/pcz076.
[25] E. Yechiel, Interactive vehicles in synergistic cosmeceuticals: advances in nanoencapsulation, transportation, transfer, and targeting, Deliv. Syst. Handb. Pers. Care Cosmet. Prod. (2005) 303–319, https://doi.org/10.1016/B978-081551504-3.50019-5.
[26] R. Pavela, Acute toxicity and synergistic and antagonistic effects of the aromatic compounds of some essential oils against Culex quinquefasciatus Say larvae, Parasitol. Res. 114 (2015) 3835–3853, https://doi.org/10.1007/s00436-015-4614-9.
[27] F. Bray, J. Ferlay, I. Soerjomataram, R.L. Siegel, L.A. Torre, A. Jemal, Global cancer statistics 2018: GLOBOCAN estimates of incidence and mortality worldwide for 36 cancers in 185 countries, CA Cancer J. Clin. 68 (2018) 394–424, https://doi.org/10.3322/caac.21492.
[28] L. Martín-Banderas, I. Muñoz-Rubio, J. Prados, J. Álvarez-Fuentes, J.M. Calderón-Montaño, M. López-Lázaro, J.L. Arias, M.C. Leiva, M.A. Holgado, M. Fernández-Arévalo, In vitro and in vivo evaluation of Δ9-tetrahidrocannabinol/PLGA nanoparticles for cancer chemotherapy, Int. J. Pharm. 487 (2015) 205–212, https://doi.org/10.1016/J.IJPHARM.2015.04.054.
[29] H. Pan, B.H. Wang, W. Lv, Y. Jiang, L. He, Esculetin induces apoptosis in human gastric cancer cells through a cyclophilin D-mediated mitochondrial permeability transition pore associated with ROS, Chem. Biol. Interact. 242 (2015) 51–60, https://doi.org/10.1016/j.cbi.2015.09.015.
[30] M. Ernst, O.M. Grace, C.H. Saslis-Lagoudakis, N. Nilsson, H.T. Simonsen, N. Rønsted, Global medicinal uses of Euphorbia L. (Euphorbiaceae), J. Ethnopharmacol. 176 (2015) 90–101, https://doi.org/10.1016/j.jep.2015.10.025.
[31] C. Mesas, R. Martínez, R. Ortíz, M. Galisteo, M. López-Jurado, L. Cabeza, G. Perazzoli, C. Melguizo, J.M. Porres, J. Prados, Antitumor effect of the ethanolic extract from seeds of euphorbia lathyris in colorectal cancer, Nutrients 13 (2021) 566, https://doi.org/10.3390/nu13020566.
[32] Y. Masamoto, H. Ando, Y. Murata, Y. Shimoishi, M. Tada, K. Takahata, Mushroom tyrosinase inhibitory activity of esculetin isolated from seeds of Euphorbia lathyris L, Biosci. Biotechnol. Biochem. 67 (2003) 631–634, https://doi.org/10.1271/bbb.67.631.
[33] T.A. Chohan, M. Sarfraz, K. Rehman, T. Muhammad, M.U. Ghori, K.M. Khan, I. Afzal, M.S.H. Akash, A.Malik Alamgeer, T.A. Chohan, Phytochemical profiling, antioxidant and antiproliferation potential of Euphorbia milii var.: experimental analysis and in-silico validation, Saudi J. Biol. Sci. 27 (2020) 3025–3034, https://doi.org/10.1016/j.sjbs.2020.08.003.
[34] R. Arora, S. Sawney, V. Saini, C. Steffi, M. Tiwari, D. Saluja, Esculetin induces antiproliferative and apoptotic response in pancreatic cancer cells by directly binding to KEAP1, Mol. Cancer 15 (2016) 1–15, https://doi.org/10.1186/s12943-016-0550-2.
[35] P.K. Dutta, P.C. Majumder, N.L. Dutta, Synthetic approaches towards bicoumarins. Synthesis of euphorbetin and isoeuphorbetin, Tetrahedron. 31 (1975) 1167–1170. https://doi.org/10.1016/0040–4020(75)85052–6.
[36] H.Y. Zhou, J.L. Hong, P. Shu, Y.J. Ni, M.J. Qin, A new dicoumarin and anticoagulant activity from Viola yedoensis Makino, Fitoterapia 80 (2009) 283–285, https://doi.org/10.1016/j.fitote.2009.03.005.
[37] C. Liang, W. Ju, S. Pei, Y. Tang, Y. Xiao, Pharmacological activities and synthesis of esculetin and its derivatives: a mini-review, J. Lipid Res. 58 (2017) 519–528, https://doi.org/10.3390/molecules22030387.
[38] V. Garcés, A. Rodríguez-Nogales, A. González, N. Gálvez, M.E. Rodríguez-Cabezas, M.L. García-Martin, L. Gutiérrez, D. Rondón, M. Olivares, J. Gálvez, J. M. Dominguez-Vera, Bacteria-carried iron oxide nanoparticles for treatment of anemia, Bioconjug. Chem. 29 (2018) 1785–1791, https://doi.org/10.1021/acs.bioconjchem.8b00245.
[39] M. Martín, A. Rodríguez-Nogales, V. Garcés, N. Gálvez, L. Gutiérrez, J. Gálvez, D. Rondón, M. Olivares, J.M. Dominguez-Vera, Magnetic study on biodistribution and biodegradation of oral magnetic nanostructures in the rat gastrointestinal tract, Nanoscale 8 (2016) 15041–15047, https://doi.org/10.1039/c6nr04678a.
[40] T. Kubrak, S. Dresler, G. Szymczak, A. Bogucka-Kocka, Rapid determination of coumarins in plants by capillary electrophoresis, Anal. Lett. 48 (2015) 2819–2832, https://doi.org/10.1080/00032719.2015.1055573.
[41] M. Tattini, M. Di Ferdinando, C. Brunetti, A. Goti, S. Pollastri, C. Bellasio, C. Giordano, A. Fini, G. Agati, Esculetin and esculin (esculetin 6-O-glucoside) occur as inclusions and are differentially distributed in the vacuole of palisade cells in Fraxinus ornus leaves: a fluorescence microscopy analysis, J. Photochem. Photobiol. B 140 (2014) 28–35, https://doi.org/10.1016/j.jphotobiol.2014.06.012.
[42] J. Jiménez-López, M.M. El-Hammadi, R. Ortiz, M.D. Cayero-Otero, L. Cabeza, G. Perazzoli, L. Martin-Banderas, J.M. Baeyens, J. Prados, C. Melguizo, A novel nanoformulation of PLGA with high non-ionic surfactant content improves in vitro and in vivo PTX activity against lung cancer, Pharmacol. Res. 141 (2019) 451–465, https://doi.org/10.1016/j.phrs.2019.01.013.
[43] Y. Jabalera, B. Garcia-Pinel, R. Ortiz, G. Iglesias, L. Cabeza, J. Prados, C. Jimenez-Lopez, C. Melguizo, Oxaliplatin-biomimetic magnetic nanoparticle assemblies for colon cancer-targeted chemotherapy: an in vitro study, Pharmaceutics 11 (2019), E395, https://doi.org/10.3390/pharmaceutics11080395.
[44] A.B. Bialkowska, A.M. Ghaleb, M.O. Nandan, V.W. Yang, Improved swiss-rolling technique for intestinal tissue preparation for immunohistochemical and immunofluorescent analyses, J. Vis. Exp. JoVE (2016), https://doi.org/10.3791/54161.
[45] K. Doello, A new pentachrome method for the simultaneous staining of collagen and sulfated mucopolysaccharides, Yale J. Biol. Med. 87 (2014) 341–347.
[46] C.S. Gai, J. Lu, C.J. Brigham, A.C. Bernardi, A.J. Sinskey, Insights into bacterial CO_2 metabolism revealed by the characterization of four carbonic anhydrases in Ralstonia eutropha H16, AMB Express 4 (2014) 2, https://doi.org/10.1186/2191-0855-4-2.
[47] D.R. Talham, Biomineralization: Principles and Concepts in Bioinorganic Materials Chemistry Stephen Mann. Oxford University Press, New York, 2001., Cryst. Growth Des. 2 (2002) 675–675. https://doi.org/10.1021/cg020033l.
[48] J. Gómez-Morales, M. Iafisco, J.M. Delgado-López, S. Sarda, C. Drouet, Progress on the preparation of nanocrystalline apatites and surface characterization: Overview of fundamental and applied aspects, Prog. Cryst. Growth Charact. Mater. 59 (2013) 1–46, https://doi.org/10.1016/j.pcrysgrow.2012.11.001.
[49] A.S. Posner, F. Betts, Synthetic amorphous calcium phosphate and its relation to bone mineral structure, Acc. Chem. Res. 8 (1975) 273–281, https://doi.org/10.1021/ar50092a003.
[50] G.B. Ramírez-Rodríguez, G. Dal Sasso, F.J. Carmona, C. Miguel-Rojas, A. Pérez-De-Luque, N. Masciocchi, A. Guagliardi, J.M. Delgado-López, Engineering biomimetic calcium phosphate nanoparticles: a green synthesis of slow-release multinutrient (NPK) nanofertilizers, ACS Appl. Bio Mater. 3 (2020) 1344–1353, https://doi.org/10.1021/acsabm.9b00937.
[51] P. Ivanchenko, J.M. Delgado-López, M. Iafisco, J. Gómez-Morales, A. Tampieri, G. Martra, Y. Sakhno, On the surface effects of citrates on nano-apatites: Evidence of a decreased hydrophilicity, Sci. Rep. 7 (2017) 1–10, https://doi.org/10.1038/s41598-017-09376-x.
[52] D.A. Long, Infrared and Raman characteristic group frequencies. Tables and charts George Socrates John Wiley and Sons, Ltd, Chichester, Third Edition, 2001. Price £135, J. Raman Spectrosc. 35 (2004) 905. https://doi.org/doi:10.1002/jrs.1238.D. A. Long. Infrared and Raman characteristic group frequencies. Tables and charts George Socrates John Wiley and Sons, Ltd, Chichester, Third Edition, 2001 Price £135, J. Raman Spectrosc. 35 2004 905 doi: 10.1002/jrs.1238.

[53] D.L. Setyaningrum, S. Riyanto, A. Rohman, Analysis of corn and soybean oils in red fruit oil using FTIR spectroscopy in combination with partial least square, Int. Food Res. J. 20 (2013) 1977–1981.
[54] Y.Y. Hu, A. Rawal, K. Schmidt-Rohr, Strongly bound citrate stabilizes the apatite nanocrystals in bone, Proc. Natl. Acad. Sci. U. S. A. 107 (2010) 22425–22429, https://doi.org/10.1073/pnas.1009219107.
[55] Y.J. Choi, C.M. Lee, S.-H. Park, M.J. Nam, Esculetin induces cell cycle arrest and apoptosis in human colon cancer LoVo cells, Environ. Toxicol. 34 (2019) 1129–1136, https://doi.org/10.1002/tox.22815.
[56] A.D. Kim, X. Han, M.J. Piao, S.R.K.M. Hewage, C.L. Hyun, S.J. Cho, J.W. Hyun, Esculetin induces death of human colon cancer cells via the reactive oxygen species-mediated mitochondrial apoptosis pathway, Environ. Toxicol. Pharmacol. 39 (2015) 982–989, https://doi.org/10.1016/j.etap.2015.03.003.
[57] X. Wang, C. Yang, Q. Zhang, C. Wang, X. Zhou, X. Zhang, S. Liu, In vitro anticancer effects of esculetin against human leukemia cell lines involves apoptotic cell death, autophagy, G0/G1 cell cycle arrest and modulation of Raf/MEK/ERK signalling pathway, J. BUON Off. J. Balk. Union, Oncol 24 (2019) 1686–1691.
[58] F. Schlenk, S. Werner, M. Rabel, F. Jacobs, C. Bergemann, J.H. Clement, D. Fischer, Comprehensive analysis of the in vitro and ex ovo hemocompatibility of surface engineered iron oxide nanoparticles for biomedical applications, Arch. Toxicol. 91 (2017) 3271–3286, https://doi.org/10.1007/s00204-017-1968-z.
[59] M. Benej, S. Pastorekova, J. Pastorek, Carbonic anhydrase IX: regulation and role in cancer, Subcell. Biochem 75 (2014) 199–219, https://doi.org/10.1007/978-94-007-7359-2_11.
[60] W. Na, Y.-H. Kang, Aesculetin inhibits bone resorption through down-regulating differentiation and lysosomal formation in osteoclasts, Curr. Dev. Nutr. 4 (2020) 442, https://doi.org/10.1093/cdn/nzaa045_075.
[61] K.H. Min, H.J. Lee, K. Kim, I.C. Kwon, S.Y. Jeong, S.C. Lee, The tumor accumulation and therapeutic efficacy of doxorubicin carried in calcium phosphate-reinforced polymer nanoparticles, Biomaterials 33 (2012) 5788–5797, https://doi.org/10.1016/j.biomaterials.2012.04.057.
[62] C. Mesas, R. Martínez, K. Doello, R. Ortiz, M. López-Jurado, F. Bermúdez, F. Quiñonero, J. Prados, J.M. Porres, C. Melguizo, In vivo antitumor activity of Euphorbia lathyris ethanol extract in colon cancer models, Biomed. Pharmacother. 149 (2022), 112883, https://doi.org/10.1016/j.biopha.2022.112883.
[63] L. Pruccoli, F. Morroni, G. Sita, P. Hrelia, A. Tarozzi, Esculetin as a bifunctional antioxidant prevents and counteracts the oxidative stress and neuronal death induced by amyloid protein in SH-SY5Y cells, Antioxid. Basel Switz. 9 (2020), E551, https://doi.org/10.3390/antiox9060551.
[64] D. Luo, X. Xu, M.Z. Iqbal, Q. Zhao, R. Zhao, J. Farheen, Q. Zhang, P. Zhang, X. Kong, siRNA-loaded hydroxyapatite nanoparticles for KRAS gene silencing in anti-pancreatic cancer therapy, Pharmaceutics 13 (2021) 1428, https://doi.org/10.3390/pharmaceutics13091428.
[65] L. Ansari, M. Derakhshi, E. Bagheri, N. Shahtahmassebi, B. Malaekeh-Nikouei, Folate conjugation improved uptake and targeting of porous hydroxyapatite nanoparticles containing epirubicin to cancer cells, Pharm. Dev. Technol. 25 (2020) 601–609, https://doi.org/10.1080/10837450.2020.1725045.
[66] N. Fatima, U. Akcan, M. Kaya, R. Gromnicova, J. Loughlin, B. Sharrack, D. Male, Tissue distribution and cellular localization of gold nanocarriers with bound oligonucleotides, Nanomed 16 (2021) 709–720, https://doi.org/10.2217/nnm-2020-0469.
[67] A.S. Drozdov, P.I. Nikitin, J.M. Rozenberg, Systematic review of cancer targeting by nanoparticles revealed a global association between accumulation in tumors and spleen, Int. J. Mol. Sci. 22 (2021) 13011, https://doi.org/10.3390/ijms222313011.
[68] E. Ansaldo, L.C. Slayden, K.L. Ching, M.A. Koch, N.K. Wolf, D.R. Plichta, E. M. Brown, D.B. Graham, R.J. Xavier, J.J. Moon, G.M. Barton, Akkermansia muciniphila induces intestinal adaptive immune responses during homeostasis, Science 364 (2019) 1179–1184, https://doi.org/10.1126/science.aaw7479.
[69] Z. Wu, S. Huang, T. Li, N. Li, D. Han, B. Zhang, Z.Z. Xu, S. Zhang, J. Pang, S. Wang, G. Zhang, J. Zhao, J. Wang, Gut microbiota from green tea polyphenol-dosed mice improves intestinal epithelial homeostasis and ameliorates experimental colitis, Microbiome 9 (2021) 184, https://doi.org/10.1186/s40168-021-01115-9.
[70] J. Fuhren, M. Schwalbe, J. Boekhorst, C. Rösch, H.A. Schols, M. Kleerebezem, Dietary calcium phosphate strongly impacts gut microbiome changes elicited by inulin and galacto-oligosaccharides consumption, Microbiome 9 (2021) 218, https://doi.org/10.1186/s40168-021-01148-0.